

RHAPSODY: I. STRUCTURAL PROPERTIES AND FORMATION HISTORY FROM A STATISTICAL SAMPLE OF RE-SIMULATED CLUSTER-SIZE HALOS

HAO-YI WU,^{1,2} OLIVER HAHN,¹ RISA H. WECHSLER,¹ YAO-YUAN MAO,¹ PETER S. BEHROOZI¹

¹Kavli Institute for Particle Astrophysics and Cosmology; Physics Department, Stanford University, Stanford, CA 94305
SLAC National Accelerator Laboratory, Menlo Park, CA 94025

²Physics Department, The University of Michigan, Ann Arbor, MI 48109; hywu@umich.edu

Draft version December 11, 2022

ABSTRACT

We present the first results from the RHAPSODY cluster re-simulation project: a sample of 96 “zoom-in” simulations of dark matter halos of $10^{14.8 \pm 0.05} h^{-1} M_{\odot}$, selected from a $1 h^{-3} \text{Gpc}^3$ volume. This simulation suite is the first to resolve this many halos with $\sim 5 \times 10^6$ particles per halo in the cluster-mass regime, allowing us to statistically characterize the distribution of and correlation between halo properties at fixed mass. We focus on the properties of the main halos and how they are affected by formation history, which we track back to $z = 12$, over five decades in mass. We give particular attention to the impact of the formation history on the density profiles of the halos. We find that the deviations from the Navarro–Frenk–White (NFW) model and the Einasto model depend on formation time. Late-forming halos tend to have considerable deviations from both models, partly due to the presence of massive subhalos, while early-forming halos deviate less but still significantly from the NFW model and are better described by the Einasto model. We find that the halo shapes depend only moderately on formation time. Departure from spherical symmetry impacts the density profiles through the anisotropic distribution of massive subhalos. Further evidence of the impact of subhalos is provided by analyzing the phase-space structure. A detailed analysis of the properties of the subhalo population in RHAPSODY is presented in a companion paper.

Keywords: cosmology: theory — dark matter — galaxies: clusters: general — galaxies: halos — methods: N-body simulations

1. INTRODUCTION

Galaxy clusters are powerful probes of cosmological parameters and have played a key role in the development of the current Λ CDM paradigm (see, e.g., Allen et al. 2011 for a review). For example, the spatial distribution and abundance of galaxy clusters reflect the growth rate of large-scale structure and the expansion rate of the universe, providing constraints on dark matter and dark energy (e.g., Vikhlinin et al. 2009; Mantz et al. 2010b; Rozo et al. 2010a), neutrino mass (e.g., Mantz et al. 2010a; Reid et al. 2010), and the validity of general relativity on cosmic scales (e.g., Rapetti et al. 2010, 2012). In the near future, the massive influx of multi-wavelength data (e.g., SPT¹, ACT², Planck³, eRosita⁴, PanSTARRS⁵, DES⁶, Euclid⁷, LSST⁸) will greatly enhance the sample size of galaxy clusters and reduce the statistical uncertainties in cluster cosmology. However, the constraining power of galaxy clusters will depend on how well various systematic uncertainties can be controlled, including the relations between observable properties and mass (e.g., Rozo et al. 2012); the robustness of cluster identification and centering (e.g., Rykoff et al. 2012); and the effect of

viewing angle and projection (e.g., White et al. 2010).

One essential way to understand these systematic uncertainties is through N-body simulations, which have been applied to study galaxy clusters for more than a decade (e.g., Tormen et al. 1997; Moore et al. 1998; Ghigna et al. 1998; also see Kravtsov & Borgani 2012 for a more general review). In the era of large-sky survey and precision cosmology, it is desirable to have controlled simulation samples that can help us understand the *statistical distribution* of the properties of galaxy clusters and the *correlation* between observables, as well as their detailed structures and evolution. Since massive galaxy clusters are rare, cosmological simulations need to cover a large volume to include a fair number of these systems (e.g., the MultiDark simulation [Prada et al. 2011] and the recent Millennium XXL simulation [Angulo et al. 2012]). However, given limited computational resources, the detailed substructures of halos are not well-resolved in these simulations. Instead of using a cosmological volume with a single resolution, one can focus on particular systems and re-simulate them with higher resolution. This so-called “zoom-in” technique provides a powerful way to study individual cluster systems in detail in a cosmological context (e.g., Tormen et al. 1997; Moore et al. 1999; Navarro et al. 2004; Gao et al. 2005; Reed et al. 2005). Nevertheless, so far most zoom-in simulations have focused only on a small number of cluster-size systems (e.g., the current high-resolution Phoenix simulation [Gao et al. 2012]) and galactic halos (e.g., the Via Lactea II simulation [Diemand et al. 2008] and the Aquarius simulations [Springel et al. 2008]). Therefore, few statements have been made about the statistical properties of well-resolved subhalos

¹ The South Pole Telescope; <http://pole.uchicago.edu/>

² Atacama Cosmology Telescope; <http://www.princeton.edu/act/>

³ <http://www.esa.int/planck>

⁴ Extended ROentgen Survey with an Imaging Telescope Array; <http://www.mpe.mpg.de/eROSITA>

⁵ The Panoramic Survey Telescope & Rapid Response System; <http://pan-starrs.ifa.hawaii.edu/>

⁶ The Dark Energy Survey; <http://www.darkenergysurvey.org/>

⁷ <http://sci.esa.int/euclid/>

⁸ The Large Synoptic Survey Telescope; <http://www.lsst.org/>

in the mass regime of galaxy clusters.

In this work, we perform re-simulations of a large number of cluster-forming regions in a cosmological volume (side length $1 h^{-1}\text{Gpc}$) to create a high-resolution statistical cluster sample, RHAPSODY, which stands for “Re-simulated HALo Population for Statistical Observable-mass Distribution study”. The current sample includes 96 halos of mass $10^{14.8 \pm 0.05} h^{-1} M_{\odot}$ with mass resolution $1.3 \times 10^8 h^{-1} M_{\odot}$. One of the main goals of RHAPSODY is to create a sample of cluster-size halos at fixed mass that enables us to make statistical statements about the halo population that is relevant for current and imminent cluster surveys.

In Figure 1, we compare RHAPSODY 8K (main sample) and RHAPSODY 4K (a factor of 8 lower in mass resolution) to several N-body simulations in the literature (Millennium II [Boylan-Kolchin et al. 2009]; Millennium XXL [Angulo et al. 2012]; Bolshoi [Klypin et al. 2011]; MultiDark [Prada et al. 2011]; Consuelo and Carmen [from LasDamas; McBride et al. in preparation]; Phoenix [Gao et al. 2012]; Aquarius [Springel et al. 2008]). Halos from zoom-in simulations are presented by symbols, while halo populations inside cosmological volumes are presented by curves with the shape of the halo mass function. RHAPSODY is in a unique regime in terms of the number of halos in a narrow mass bin simulated with high particle number. It is also worth noting that RHAPSODY is currently the largest sample of halos with more than a few times 10^6 particles per halo at any given mass in the literature. Our repeated implementation of the re-simulation method makes the simulation suite statistically interesting and computationally feasible.

The RHAPSODY sample is highly relevant to several current observational programs. For example, the galaxy cluster catalogs from the SDSS (Koester et al. 2007; Hao et al. 2010) include many tens of thousands of photometrically-selected clusters and have provided a rich sample for multi-wavelength mass calibration (Rozo et al. 2010b; Rykoff et al. 2012), cosmological constraints (Rozo et al. 2007, 2010a), and studies of the cluster galaxy populations (Hansen et al. 2009). The Cluster Lensing And Supernova survey with Hubble Multi-Cycle Treasury Program (CLASH; Postman et al. 2011) focuses on 25 massive clusters and aims to establish unbiased measurements of cluster mass-concentration relation of these clusters. Recently, von der Linden et al. (2012) published accurate weak lensing mass calibrations of 51 massive clusters, focusing on understanding various systematics for cluster count experiments. In addition, various X-ray programs have been efficiently identifying massive clusters; for example, the ROSAT Brightest Cluster Sample (Ebeling et al. 2000), the ROSAT-ESO Flux-Limited X-ray sample (Böhringer et al. 2004), and the MAssive Cluster Survey (Ebeling et al. 2010). These samples have achieved high completeness and provided a relatively unbiased selection. Relatively recently, massive galaxy clusters have also been detected through the Sunyaev-Zel’dovich (SZ) effect by ACT (Marriage et al. 2011), SPT (Williamson et al. 2011), and Planck (Planck Collaboration et al. 2011). These detections have ushered in an era of high-purity detection of high-redshift galaxy clusters. The RHAPSODY sample is in a mass regime similar to these observational programs and can provide a statistical description of the dark matter halos associated with these clusters.

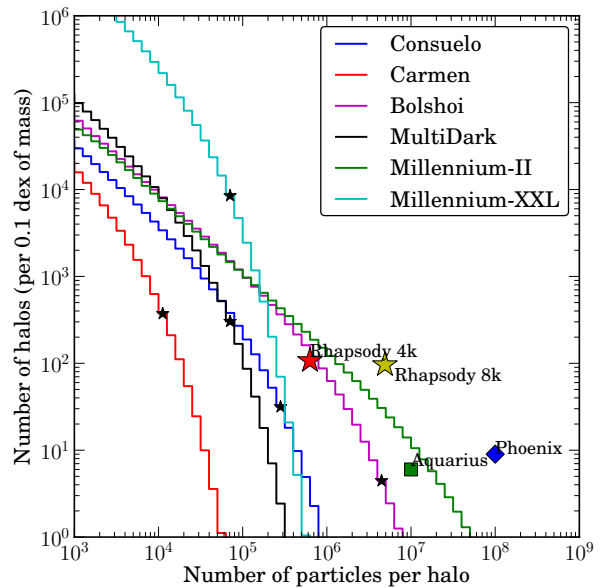


Figure 1. Comparison of the halo samples in various N-body simulations; RHAPSODY is in a unique statistical regime of well-resolved massive halos. The number of halos (per 0.1 dex in mass) is shown as a function of number of particles inside the virial radius of the halo. Symbols correspond to halos in re-simulation projects; the RHAPSODY 4K and 8K samples are shown as two colored stars ($M_{\text{vir}} = 10^{14.8 \pm 0.05} h^{-1} M_{\odot}$). Curves correspond to halos in different cosmological volumes, and black stars on these curves correspond to the number of halos of the same mass as RHAPSODY. We note that Consuelo and Carmen both include 50 volumes, and only one volume is presented here.

This paper presents the first results from the RHAPSODY simulations. We first characterize the formation history and the density profiles of the 96 main halos. We then explore how formation history impacts halo concentration and the deviation from the Navarro-Frenk-White (NFW) profile. We find that the deviations from the NFW model systematically depend on formation time and are impacted by the presence of massive subhalos.

We connect the density profile to the phase-space structures of halos and find that late-forming halos tend to have outflows within R_{vir} , which can be also be attributed to massive subhalos. We have also investigated the shape parameters for the spatial distributions and velocities of dark matter particles. We find that the shape parameters, after removing massive subhalos, have no strong correlation with formation time, indicating that the deviation from spherical symmetry alone cannot account for the trend of profile and formation time.

This paper is organized as follows. In §2, we detail the simulations. We present the formation history of the main halos in §3.1 and merger rate in §3.2. In §4.1, we present the density profiles and compare various fitting functions; in §4.2, we demonstrate the effect of formation history on the density profile. In §5, we analyze the impact of formation time on the phase-space structure. The shapes of spatial distributions and velocities of dark matter particles and their alignments are discussed in §6. We conclude in §7.

In a second paper in this series (Wu et al. 2012, hereafter Paper II), we will present the properties of subhalos in our sample and the impact of formation time on them,

which is more complex in the sense that the subhalo properties depend on the selection method of subhalos, the stripping experienced by a subhalo, and the resolution of the simulation.

2. THE SIMULATIONS

The RHAPSODY sample includes 96 cluster-size halos of mass $M_{\text{vir}} = 10^{14.8 \pm 0.05} h^{-1} M_{\odot}$, re-simulated from a cosmological volume of $1 h^{-1} \text{Gpc}$. Each halo was simulated at two resolutions: $1.3 \times 10^8 h^{-1} M_{\odot}$ (equivalent to 8192^3 particles in this volume), which we refer to as ‘‘RHAPSODY 8K’’ or simply ‘‘RHAPSODY’’; and $1.0 \times 10^9 h^{-1} M_{\odot}$ (equivalent to 4096^3 particles in this volume), which we refer to as ‘‘RHAPSODY 4K.’’ These two sets allow detailed studies of the impact of resolution. The simulation parameters are summarized in Table 1.

The initial conditions were generated with the multi-scale initial condition generator MUSIC (Hahn & Abel 2011). The particles were then evolved using the public version of GADGET-2 (Springel 2005). The halo finding was performed with the phase-space halo finder ROCKSTAR (Behroozi et al. 2011a). Finally, merger trees were constructed with the gravitationally-consistent code of Behroozi et al. (2011b). We provide more details on our methods below.

All simulations in this work are based on a Λ CDM cosmology with density parameters $\Omega_m = 0.25$, $\Omega_{\Lambda} = 0.75$, $\Omega_b = 0.04$, spectral index $n_s = 1$, normalization $\sigma_8 = 0.8$, and Hubble parameter $h = 0.7$.

Figure 2 shows the images of 90 halos at $z = 0$ in the RHAPSODY 8K sample. Halos are sorted by their concentration and subhalo number, as described in the following sections. Figure 3 shows the evolution of 4 individual halos, selected as extremes in the distribution of concentration and subhalo number. Movies and images for each individual halo are available at <http://risa.stanford.edu/rhapsody/>.

2.1. The cosmological volume

Our re-simulations are based on one of the CARMEN simulations from the LArge Suite of DArk MATter Simulations (LASDAMAS; McBride et al.). The simulation represents a cosmological volume of $1 h^{-1} \text{Gpc}$ with 1120^3 particles. Its initial conditions are generated with the code of Crocce et al. (2006) based on the second-order Lagrangian perturbation theory (2LPT), and the N-body simulation was run with the GADGET-2 code. RHAPSODY uses the same cosmological parameters as CARMEN.

When selecting targets for re-simulation from the massive end of the halo mass function, we choose a mass bin that is narrow enough so that mass trends of halo properties are negligible but at the same time wide enough to include a sufficient number of halos for statistical analyses. Here we focus on a 0.1 dex bin surrounding $\log_{10} M_{\text{vir}} = 14.8$. This mass range allows us to select ~ 100 halos in a narrow mass range, and is well-matched to the masses of the massive clusters studied in X-ray, SZ, and optical cluster surveys.

2.2. Initial conditions

For each of the halos in our sample, we generate multi-resolution initial conditions using the MUSIC code (Hahn & Abel 2011). We use the same white noise field of CARMEN (1024^3 of its 1120^3 modes) to generate the large-scale

perturbations consistent with CARMEN. The equivalent resolution ranges from 256^3 in the lowest resolution region to 8192^3 (4096^3 for the 4K sample) in the highest resolution region. In between, the mass resolution changes by factors of 8 every 8 times the mean inter-particle distance.

For each of our re-simulation targets, we choose a zoom-in volume that is 40% larger than the Lagrangian volume of the friends-of-friends halo at $z = 0$. This choice has been tested to provide a well-converged dark matter density profile in our convergence tests. With this setting, no low-resolution particle was found within the virial radius of any targeted halo. The typical number of high resolution particles per simulation is thus about $42/5.4$ million for 8K/4K with a standard deviation of 18%.

In MUSIC, particle displacements and velocities have been computed from the multi-scale density field using 2LPT at a starting redshift of 49, in accordance with CARMEN. The use of 2LPT is important for statistical studies of such massive systems since their masses depend on the accuracy of the initial conditions (e.g., Crocce et al. 2006; Tinker et al. 2008; Reed et al. 2012; Behroozi et al. 2012; and McBride et al., in preparation).

2.3. Gravitational evolution

After generating the initial conditions, we evolve each cluster-forming region using the public version of the GADGET-2 code (Springel 2005). Gravitational forces are computed using two levels of particle-mesh together with the force tree to achieve a force resolution of comoving $3.3/6.7 h^{-1} \text{kpc}$ in the RHAPSODY 8K/4K for particles in the high resolution region. For each simulation, we save 200/100 snapshots logarithmically spaced in scale factor a between $a = 0.075$ and $a = 1$ for the 8K/4K sample.

We note that the virial masses of the re-simulated halos change somewhat with the improved resolution. As a result, a fraction of the halos fall outside the narrow targeted mass range $\log_{10} M_{\text{vir}} = 14.8 \pm 0.05$. In most cases, the masses scatter slightly upwards. We discard those halos falling outside the targeted mass bin of RHAPSODY to keep the mass selection clean. In principle, to obtain all halos in the 14.8 ± 0.05 mass bin in the re-simulated sample, one needs to re-simulate a wider range of masses around 14.8 to include all halos that end up in the targeted bin. However, the large suite of re-simulations thus required is beyond the scope of this work. Thus, we note that RHAPSODY does not strictly include the complete sample of halos within $\log_{10} M_{\text{vir}} = 14.8 \pm 0.05$ in either the original volume or the re-simulations. However, we do not expect this fact to affect the results presented in this paper, because the main approach in this paper is stacking all halos in RHAPSODY for sufficient statistics and our sample should be unbiased. Global statistics for halos in this bin in the entire cosmological volume (for example, the two-point correlation function) are not used in the present work.

2.4. Halo and subhalo identification

Our simulations are post-processed with the adaptive phase-space halo finder ROCKSTAR (Behroozi et al. 2011a), which can achieve high completeness in finding subhalos even in dense environments (see also Knebe et al. 2011). Based on the phase-space information, small subhalos passing through the dense central region of the

Type	Name	Mass Resolution [$h^{-1}M_{\odot}$]	Force Resolution [$h^{-1}\text{kpc}$]	Number of Particles in Simulation	Number of Particles in Each Targeted Halo
Full Volume	CARMEN	4.94×10^{10}	25	1120 ³	12K
Zoom-in	RHAPSODY 4K	1.0×10^9	6.7	$5.4M^a / 4096^3$ (<i>equiv.</i>)	$0.63M^b$
	RHAPSODY 8K	1.3×10^8	3.3	$42M^a / 8192^3$ (<i>equiv.</i>)	$4.9M^b$

^aThe mean number of high-resolution particles in each zoom-in region.

^bThe mean number of high-resolution particles within the R_{vir} of each targeted halo.

Table 1
Simulation parameters.

main halo can be robustly identified. This feature is especially important for studying the subhalo populations, which we focus on in Paper II. We note that the algorithm is only applied to high-resolution particles in the simulations.

ROCKSTAR pays special attention to major merger events (two halos of similar mass merge with each other), which arise frequently in the formation history of RHAPSODY halos (because of their high masses) and often cause difficulties in the construction of merger trees. During a major merger between two halos, a large fraction of dark matter particles appear as unbound to either of the merging halos, even though they are bound to the entire merging system. Therefore, regular unbinding procedures tend to result in ambiguities or inconsistencies in halo mass assignment. ROCKSTAR addresses this issue by computing the gravitational potential of the entire merging system, thus making the mass evolution of halos self-consistent across time steps.

2.5. Merger trees

We apply the gravitationally-consistent merger tree algorithm developed by Behroozi et al. (2011b) to the 200/100 output snapshots which were saved between $z = 12.3$ and $z = 0$ for RHAPSODY 8K/4K. The idea behind this new merger tree implementation is that the stochasticity in N-body simulations often leads to failures in halo finding. For example, the halo finder might find a spurious halo that is in reality a random density fluctuation at a certain time step, or the halo finder might miss a halo because it falls below the detection threshold at that particular time step. Given these limitations in halo finders, previous implementations of merger trees often encounter problems in linking halos across different time steps. The gravitationally-consistent merger tree algorithm resolves this issue by comparing adjacent time steps to recover missing subhalos and remove spurious halos, thereby improving the completeness and purity of the halo catalogs and ensuring correct linking of halos across time steps. This algorithm compares two adjacent time steps and can be summarized as follows: (1) It takes the halos at the later time step and evolves their positions and velocities backward in time, deciding whether the progenitors are missing or incorrectly linked. (2) It takes the halos at the earlier time step and looks for its descendant in the later time step. If the descendant is missing, the algorithm decides whether a merger occurs or the current halo is spurious. For details of the implementation, we refer the reader to Behroozi et al. (2011b).

2.6. Summary of halo properties

In Table 2, we summarize the key halo properties discussed throughout this paper. In Figure 4, we present the distributions of and correlations between several of these

properties. We use the *rank correlations* throughout this work to avoid the impact of outliers.

In this work, the halo mass definition is based on the spherical overdensity of virialization, Δ_{vir} , with respect to the critical density, ρ_{crit} . We use the center of the phase-space density peak calculated by ROCKSTAR as the center of a halo. Based on this center, we draw a sphere with radius R_{vir} so that the mean overdensity enclosed is equal to $\Delta_{\text{vir}}\rho_{\text{crit}}$. With the cosmological parameters used herein, $\Delta_{\text{vir}} = 94$ with respect to the critical density at $z = 0$ (Bryan & Norman 1998); i.e., $\Delta_{\text{vir}} = \Delta_{94c} = \Delta_{376m}$. The subscripts c and m indicate the overdensities with respect to the critical density and mean matter density. For reference, in Table 2 we list halo masses and radii based on several commonly-used overdensity values: $\Delta_{200m} = \Delta_{50c}$, Δ_{200c} , $\Delta_{500m} = \Delta_{125c}$, and Δ_{500c} .

In Table 2, we list two properties that are closely related to halo mass: the maximum circular velocity and the velocity dispersion of dark matter particles. The maximum circular velocities is defined at a radius r_{max} that maximizes $\sqrt{GM(<r)}/r$:

$$v_{\text{max}} = \sqrt{\frac{GM(<r_{\text{max}})}{r_{\text{max}}}}. \quad (1)$$

The velocity dispersion is calculated based on dark matter particles:

$$\sigma_v^2 = \langle |\mathbf{v} - \bar{\mathbf{v}}|^2 \rangle = \frac{1}{N_p} \sum_{i=1}^{N_p} |\mathbf{v}_i - \bar{\mathbf{v}}|^2. \quad (2)$$

We note that the correlation between M_{vir} and σ_v is 0.32, indicating that there is a non-negligible residual mass-velocity dispersion scaling despite the narrow mass range of our sample. For this reason, in the remainder of the paper, we have always verified carefully that the quoted correlations between various properties are not simply driven by mass.

3. THE BUILDUP OF CLUSTER-SIZE HALOS

In this section, we present the mass accretion history and merger rate of the main halos in RHAPSODY, paving the way for further discussions of the impact of formation time on halo properties. The formation history of dark matter halos is known to correlate with various halo properties, including their clustering, internal structure, and subhalos (e.g., Wechsler et al. 2002; Zhao et al. 2003; Harker et al. 2006; Hahn et al. 2007; Maulbetsch et al. 2007; Li et al. 2008). On the other hand, the merger rate of dark matter halos serves as a baseline for modeling several processes in galaxy formation, including the build-up of stellar mass and supermassive black holes, the star formation rate, the color and morphology evolution (e.g.,

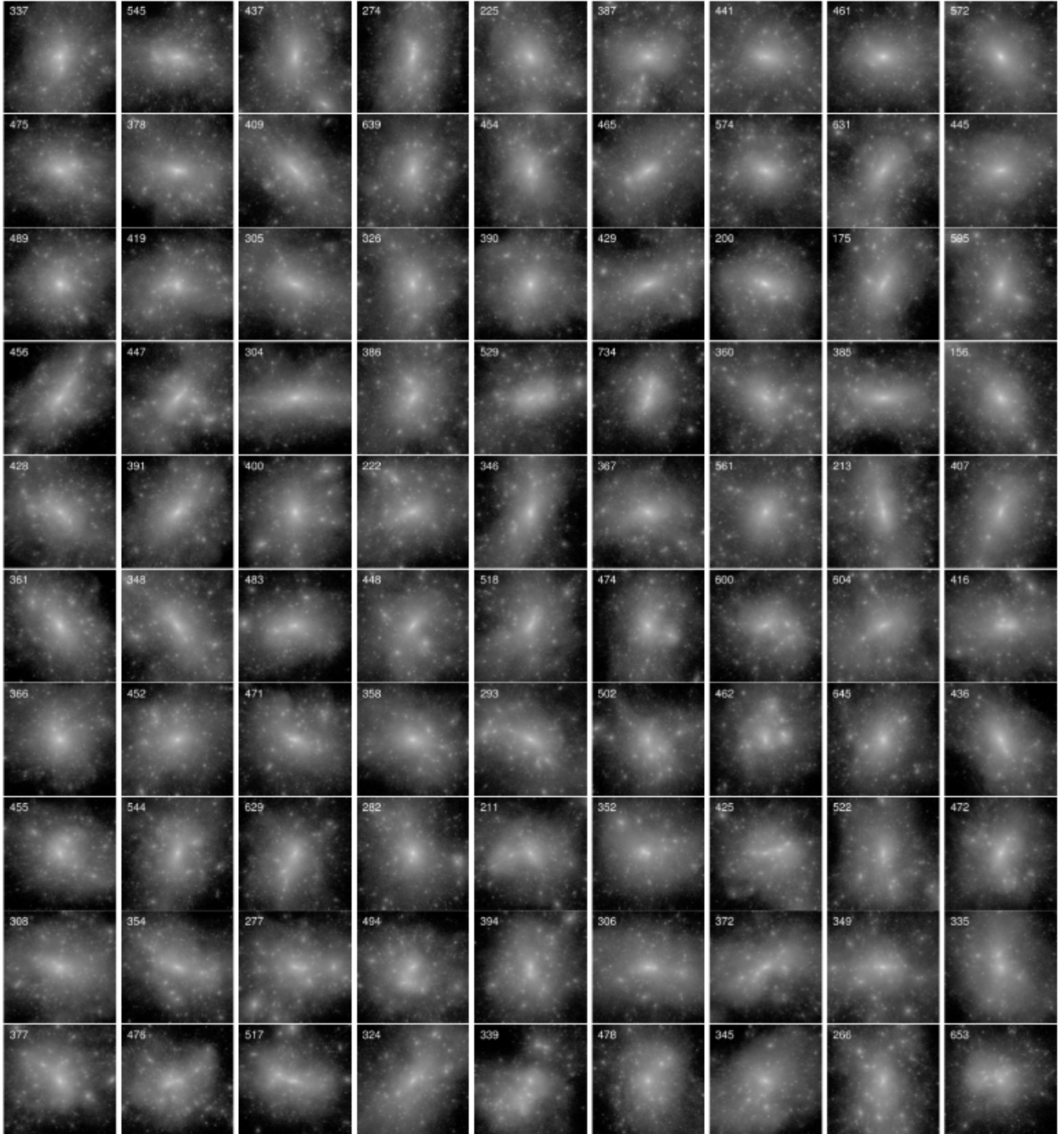


Figure 2. Images of 90 RHAPSODY halos at $z = 0$. The halos are first sorted by concentration (high concentration on the upper rows, low on the bottom). In each row, the halos are then sorted by the number of subhalos (selected with $v_{\max} > 100$ km/s, high number of subhalos on the left columns, low on the right). Each image has a physical extent of $4 h^{-1}$ Mpc on a side, which is slightly larger than the average virial radius of $1.8 h^{-1}$ Mpc.

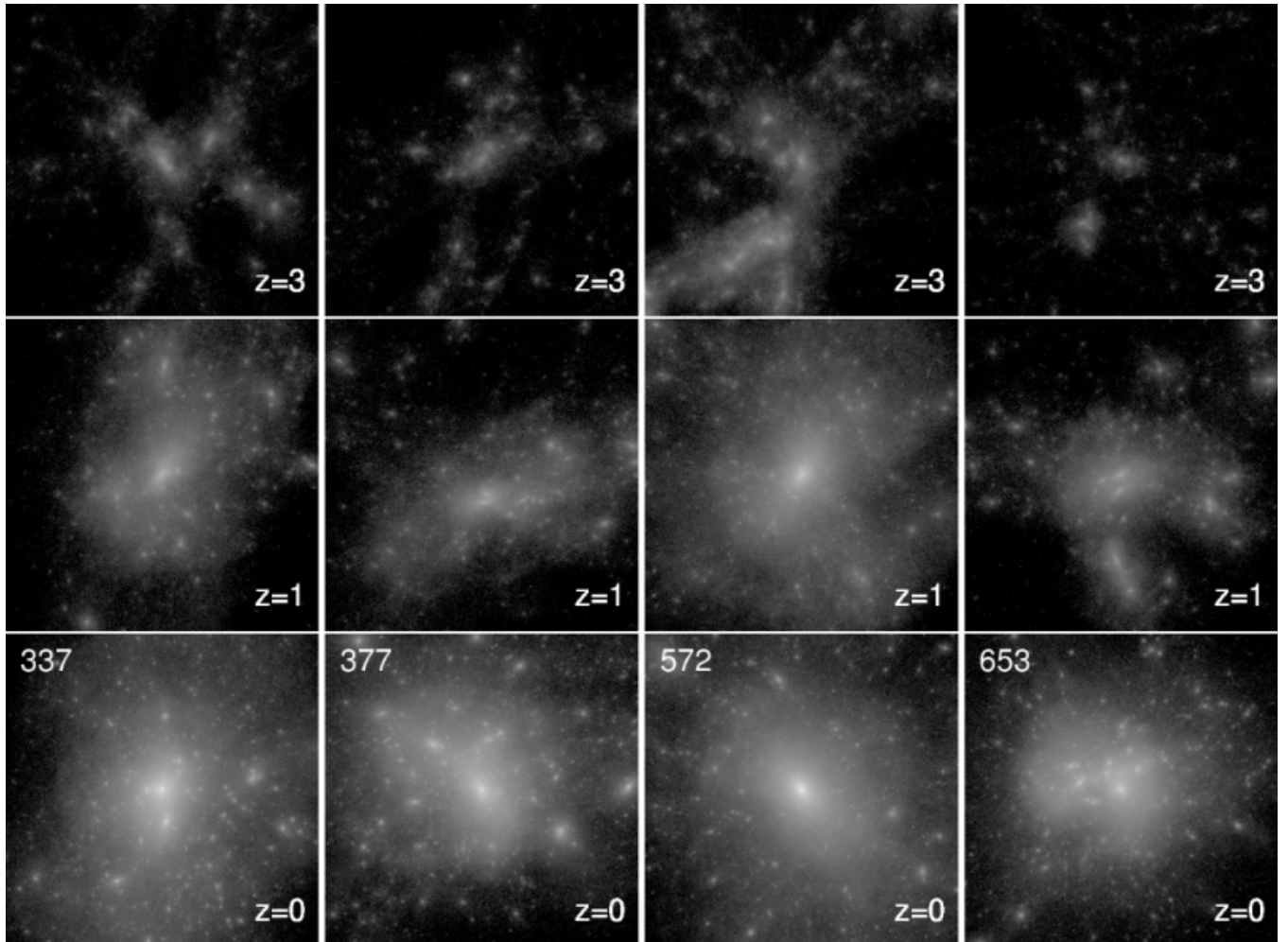


Figure 3. Evolution of four RHAPSODY halos. From top to bottom, the images show the progenitors of four halos at $z = 3$ and $z = 1$, and the halo at $z = 0$. The four halos chosen are the corners of Fig 2. From left to right, they have high concentration, high subhalo number [337]; low concentration, high subhalo number [377]; high concentration, low subhalo number [572]; low concentration, low subhalo number [653]. Halo 572 has the highest concentration, the least late-time accretion, and the most dominant central halo of our full sample. It is also the halo with the most massive progenitor at $z = 3$. Each panel has a comoving extent of $4 h^{-1}\text{Mpc}$ on a side, and is centered on the most massive progenitor in each case.

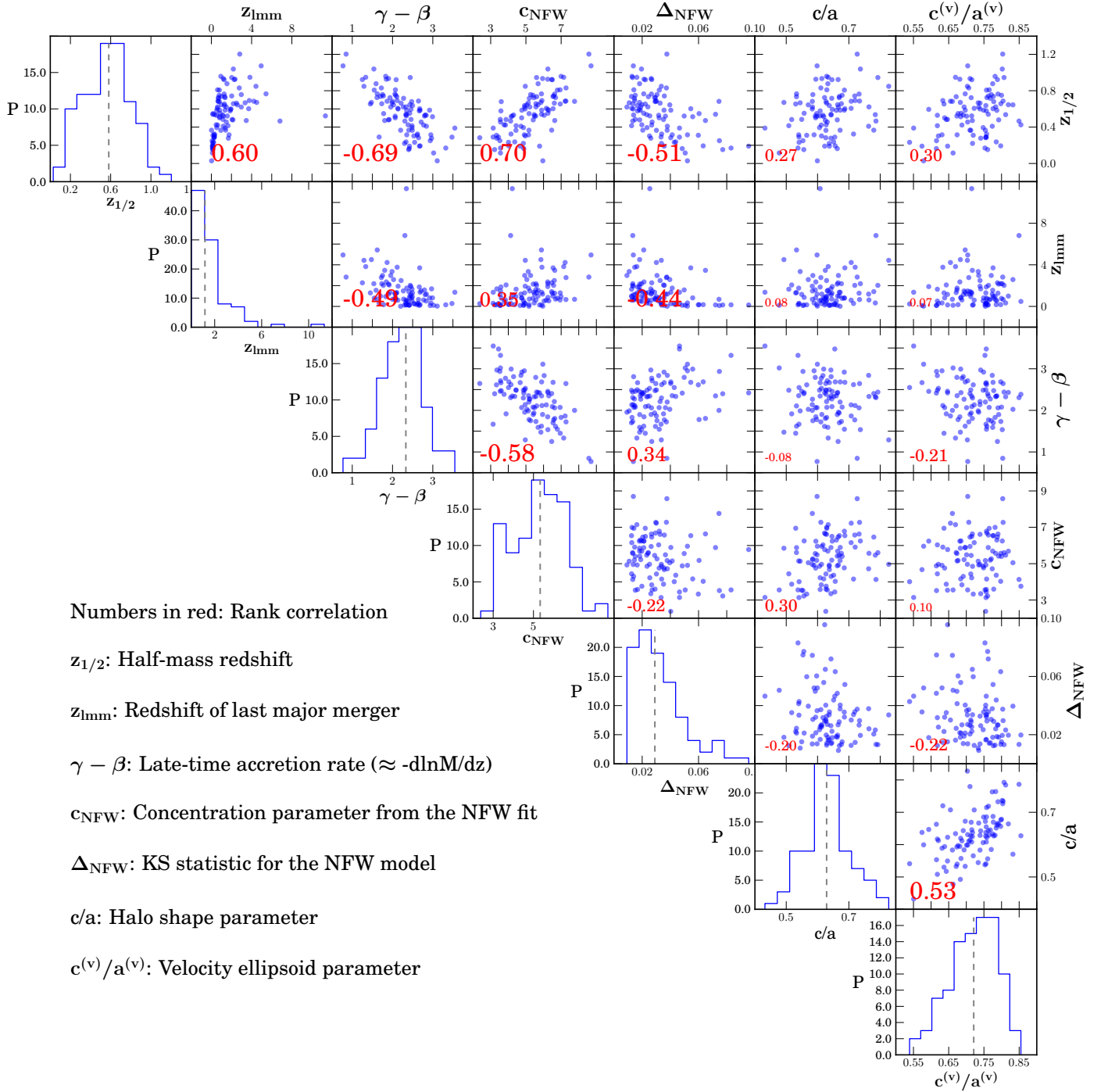


Figure 4. Distributions of and correlations between main halo properties and formation history parameters. The number in red in each panel shows the *rank correlation coefficient*, and its font size reflects the magnitude of correlation.

Property	Median	Frac. Scatter	Mean	Frac. SD	Def.
$M_{\text{vir}} [h^{-1}M_{\odot}]$	6.4×10^{14}	0.072	6.4×10^{14}	0.061	§2.6
$R_{\text{vir}} [h^{-1}\text{Mpc}]$	1.8	0.024	1.8	0.028	
$\sigma_v [\text{km/s}]$	1,400	0.041	1,400	0.039	
$v_{\text{max}} [\text{km/s}]$	1,300	0.036	1,300	0.042	
M_{200m}	7.3×10^{14}	0.083	7.3×10^{14}	0.077	$h^{-1}M_{\odot}$; §2.6
M_{200c}	5.9×10^{14}	0.065	5.9×10^{14}	0.056	
M_{500m}	5.0×10^{14}	0.063	5.0×10^{14}	0.062	
M_{500c}	3.4×10^{14}	0.13	3.4×10^{14}	0.12	
R_{200m}	2.3	0.028	2.3	0.026	$h^{-1}\text{Mpc}$; §2.6
R_{200c}	1.6	0.022	1.6	0.019	
R_{500m}	1.3	0.021	1.3	0.021	
R_{500c}	0.84	0.043	0.83	0.04	
z_{lmm}	1.2	1.1	1.6	1.1	§3.1
$z_{1/2}$	0.58	0.44	0.56	0.43	
z_{α}	0.67	0.058	0.67	0.059	
$\gamma - \beta$	2.3	0.22	2.2	0.23	
$r_s [h^{-1}\text{Mpc}]$	0.34	0.31	0.36	0.27	§4.1
cNFW	5.3	0.26	5.3	0.23	
cNFW-like	5	0.27	5.1	0.32	
cEinasto	4.9	0.23	4.9	0.28	
γ NFW-like	3.4	0.43	3.9	0.34	
γ Einasto	3	0.13	3	0.14	
α Einasto	0.24	0.42	0.27	0.41	
b/a	0.75	0.12	0.76	0.12	§6.1
c/a	0.63	0.12	0.63	0.12	
T	0.71	0.27	0.69	0.27	
$b^{(v)}/a^{(v)}$	0.82	0.096	0.82	0.093	§6.2
$c^{(v)}/a^{(v)}$	0.72	0.098	0.72	0.094	
$\delta_{\sigma_{los}^2}$	0.17	0.32	0.18	0.3	

Table 2

Properties of RHAPSODY halos at $z = 0$. The second column shows the median, the third column corresponds to the ratio of the 68% scatter to the median. The fourth column shows the sample mean and the fifth column corresponds to the ratio of the standard deviation to the mean.

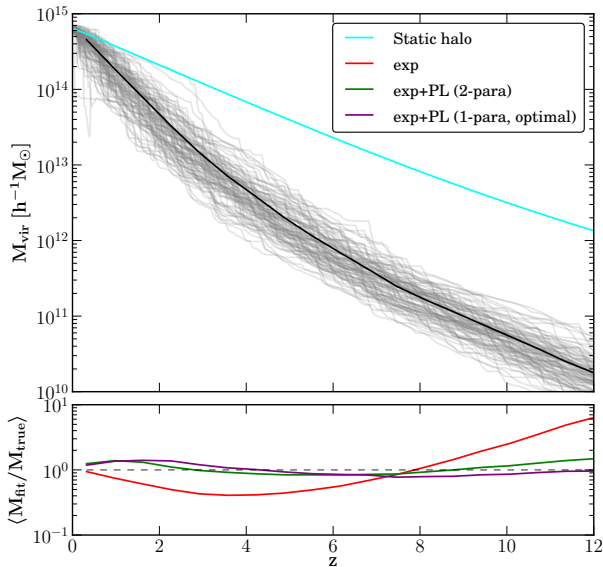


Figure 5. Mass accretion history of the main halos in RHAPSODY. The gray curves indicate the trajectories of individual halos; the black curve indicates the average over all halos. The cyan curve indicates the pseudo-evolution of a static halo. We show the virial mass of the most massive progenitor at each output redshift. The bottom panel shows the residual of the fit for three analytical models.

Kauffmann & Haehnelt 2000; Hopkins et al. 2006; De Lucia & Blaizot 2007; Behroozi et al. 2012). In addition, there has been an ongoing effort to measure merger rates in observations (e.g., Bell et al. 2006; Lotz et al. 2008; Xu et al. 2012). While a study of the implications for galaxy formation is beyond the scope of this paper, we note that the merger rate provided here can be applied to modeling galaxy formation in massive clusters.

3.1. Mass accretion history

Figure 5 presents the mass evolution of the main halos in RHAPSODY. For each main halo identified at $z = 0$, we search through its merger tree to find the most massive progenitor at each redshift. The gray curves show the evolution of M_{vir} for individual halos, and the black curve shows the average of all halos. We note that the fractional dispersion is roughly constant for all redshifts. In the upper panel, we add a cyan line showing the pseudo evolution of a static halo (with a non-evolving density profile and $M_{\text{vir}} = 10^{14.8} h^{-1} M_{\odot}$ at $z = 0$) expected simply from the evolution of Δ_{vir} and the critical density (e.g., Diemer et al. 2012).

Our halo formation histories span almost 5 orders of magnitude in mass and cover the 13.8 Gyr between $z = 12$ and $z = 0$, allowing us to test the validity of parameterizations proposed in the literature (e.g., Wechsler et al. 2002; van den Bosch 2002; Tasitsiomi et al. 2004; Zhao et al. 2009; McBride et al. 2009) over much larger ranges in both time and mass. We fit the following three models:

1. An exponential model (Wechsler et al. 2002)

$$M(z) = M_0 e^{-\alpha z} . \quad (3)$$

We note that this model assumes a constant mass ac-

cretion rate represented by the exponential growth index

$$-\frac{d \ln M}{dz} = \alpha . \quad (4)$$

The curves in Figure 5 do not follow straight lines, indicating a systematic deviation from the pure exponential model. For this model, a formation time proxy can be defined as

$$z_{\alpha} = \ln 2 / \alpha . \quad (5)$$

2. An exponential-plus-power law model with two parameters (McBride et al. 2009)

$$M(z) = M_0 (1 + z)^{\beta} e^{-\gamma z} . \quad (6)$$

We note that

$$-\frac{d \ln M}{dz} \approx \gamma - \beta \quad \text{when } z \ll 1 . \quad (7)$$

Thus, $\gamma - \beta$ can be used as a measure for the late-time accretion rate. Analogous to Equation 5, a formation time proxy can be defined as

$$z_{\gamma-\beta} = \ln 2 / (\gamma - \beta) . \quad (8)$$

One can alternatively solve $M(z_{\beta\gamma}) = M_0/2$ numerically. However, we note that $z_{\beta\gamma}$, $z_{\gamma-\beta}$, and $\gamma - \beta$ are completely correlated with each other.

3. An exponential-plus-power law model with one parameter, motivated by Equation 6. When fitting for Equation 6, we observe that the two parameters β and γ are highly correlated (see Appendix A). We thus adopt a 1-parameter model that incorporates this correlation

$$M(z) = M_0 (1 + z)^{-4.61 + 5.27\gamma} e^{-\gamma z} . \quad (9)$$

The two numerical coefficients are obtained by an optimization scheme described in Appendix A.

Our fitting procedure and the goodness-of-fit are also discussed in Appendix A. The bottom panel of Figure 5 shows the average of the residual for the individual fit, $\langle M_{\text{fit}}/M_{\text{true}} \rangle$. The pure exponential model does not provide the curvature needed to fit the data. The two exponential-plus-power law models work almost equally well, but significant residual remains for $z < 2$.

3.2. Merger rate

The merger rate experienced by a dark matter halo as a function of time and merger ratio is a specific prediction of the Λ CDM model (e.g., Press & Schechter 1974; Lacey & Cole 1993) and has been calibrated with ever-improving precision using the extended Press-Schechter model (e.g., Neistein & Dekel 2008) and N-body simulations (e.g., Fakhouri & Ma 2008; Stewart et al. 2009; Genel et al. 2009). In this work, we use the new merger tree implementation of Behroozi et al. (2011b) to re-examine the merger rate of cluster-size halos. We consider the epoch of a merger event to be the earliest redshift where a smaller halo enters the virial radius of a larger halo, and the merger ratio, $\mu = M^{\text{merging}}/M^{\text{main}}$, is defined at this epoch.

Figure 6 presents the merger rate for RHAPSODY halos. The left panel shows the cumulative merger rate:

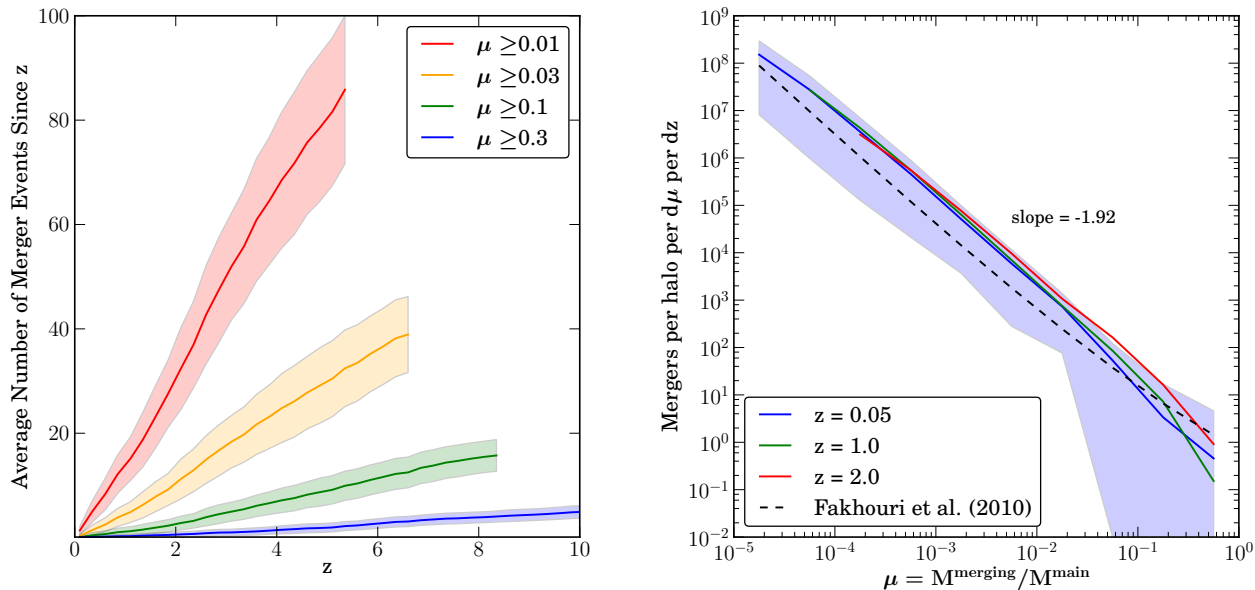


Figure 6. The merger rate of RHAPSODY halos. *Left:* Cumulative merger rate as a function of redshift (per halo). The average number of merger events each main halo has experienced since a given z is shown for three different merger mass ratios $\mu = M^{\text{merging}}/M^{\text{main}}$. *Right:* Differential merger rate as a function of merger mass ratio. The number of merger events per halo per $d\mu$ per dz is shown as a function of μ . The three different curves correspond to different redshifts, and the trend is independent of redshift. For both panels, each colored band corresponds to the standard deviation of the curve of the same color.

The x -axis specifies a look-back redshift, and the y -axis shows the average number of merger events each main halo has experienced since this redshift. Different curves correspond to different merger mass ratio thresholds, $\mu \geq 0.01, 0.03, 0.1,$ and 0.3 , and the shaded regions indicate the standard deviation of the sample. We identify the redshift of the last major merger, z_{lmm} , using $\mu \geq 0.3$. Our merger rate is consistent with the trend of the main halo mass presented in Fakhouri et al. (2010), who have used Millennium Simulations I and II and do not have sufficient statistics in our mass regime.

The right panel shows the merger rate as a function of the merger mass ratio μ . We plot the differential number of merger events each main halo has experienced, per $d\mu$ per dz , for a given merger ratio. The different colored curves represent different redshifts. We find that the merger rate trends are almost invariant with redshift. The blue shaded region corresponds to the scatter of the blue curve ($z = 0.05$) and indicates the large variation of merger rate from halo to halo. The logarithmic slope, -1.92 , is very close to the value -2 in Fakhouri & Ma (2008) and Fakhouri et al. (2010). We also plot the fitting formula in Fakhouri et al. (2010) as a black dashed curve ($z = 0.05$). While the overall slope agrees well, their normalization is slightly lower but still agrees within our error bar.

Figure 4 shows that z_{lmm} correlates with $z_{1/2}$, as well as various halo structural properties, which will be detailed in the following sections.

4. THE IMPACT OF FORMATION TIME ON THE DENSITY PROFILE

The density profiles of dark matter halos have been shown to follow the universal Navarro–Frenk–White (NFW) form (Navarro et al. 1997) and can be well characterized by the concentration parameter c . Calibrating the concentration–mass relation and its scatter has been

an ongoing effort (e.g., Bullock et al. 2001; Wechsler et al. 2006; Neto et al. 2007; Macciò et al. 2008; Gao et al. 2008; Prada et al. 2011; Bhattacharya et al. 2011) and is of increasing importance for interpreting observations. As mentioned in the introduction, the CLASH project is a major effort of the Hubble Space Telescope and aims for detailed and unbiased measurements of the density profile of galaxy clusters, which are tests of both the Λ CDM paradigm and our understanding of the assembly of clusters. In addition, the modeling of the concentration–mass relation impacts the interpretation of the weak lensing results (e.g., King & Mead 2011) and X-ray results (e.g., Ettori et al. 2010).

In this section, we first provide fits to the density profiles of the halos in the RHAPSODY sample. The halos of galaxy clusters, being the most massive objects in the universe, assemble very late in cosmic history, so that recent violent merger and accretion events are expected to impact their density profiles. For this reason, we study in detail the relation between their formation history and profiles in the remainder of the section.

4.1. Fitting the density profile

The left panel of Figure 7 shows the density profiles of the main halos in RHAPSODY. The black curve corresponds to the mean density profile, while the gray curves correspond to individual halos. We use 32 bins between $10^{-2.5}R_{\text{vir}}$ and R_{vir} equally spaced in $\log r$ for plotting these curves. We note that the difference in the binned density profile between each re-simulated halo and its low-resolution version is between 5% and 10%.

For each main halo, we use all dark matter particles between $13 h^{-1}\text{kpc}$ and R_{vir} to fit the density profile, adopting the maximum-likelihood estimation without binning in radius (explained in detail in the Appendix B).

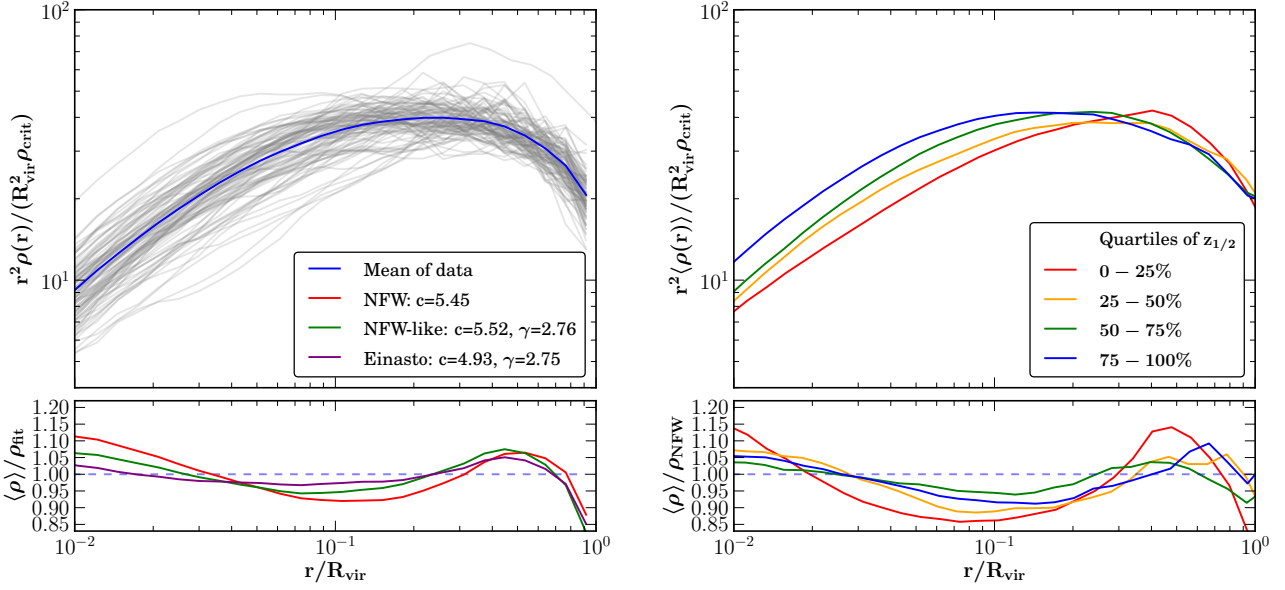


Figure 7. *Left:* Density profiles of the main halos in RHAPSODY (gray: individual halos; black: average). The bottom panel shows the residuals with respect to three models (fits to the mean profile). *Right:* The impact of formation time on density profile. Halos are binned into quartiles based on their $z_{1/2}$, and the mean of halos in each quartile is shown in the upper panel. The bottom panel shows the residuals with respect to the NFW profile. Deviations from the NFW profile are systematic, with the largest deviation seen for late-forming halos and monotonous decrease when considering halos in the earlier forming bins.

There has been an ongoing effort to quantify the deviation from NFW and to search for alternative fitting functions (e.g., Navarro et al. 2004; Merritt et al. 2006; Gao et al. 2008; Navarro et al. 2010). In this work, we fit three parameterizations:

1. The NFW profile

$$\frac{\rho(r)}{\rho_{crit}} = \frac{\delta_c}{(r/r_s)(1+r/r_s)^2}, \quad (10)$$

$$\frac{d \ln \rho}{d \ln r} = -\frac{1+3(r/r_s)}{1+(r/r_s)}, \quad (11)$$

which is characterized by one parameter $c_{\text{NFW}} = R_{\text{vir}}/r_s$.

2. An ‘‘NFW-like’’ profile with a free outer slope γ

$$\frac{\rho(r)}{\rho_{crit}} = \frac{\delta_c}{(r/r_s)(1+r/r_s)^{\gamma-1}}, \quad (12)$$

$$\frac{d \ln \rho}{d \ln r} = -\frac{1+\gamma(r/r_s)}{1+(r/r_s)}, \quad (13)$$

which reduces to the NFW profile when $\gamma = 3$. This profile can be characterized by two parameters, $\gamma_{\text{NFW-like}}$ and $c_{\text{NFW-like}} = (R_{\text{vir}}/r_s)(\gamma_{\text{NFW-like}} - 2)$. The latter is defined so that $R_{\text{vir}}/c_{\text{NFW-like}}$ equals the radius at which the density slope is -2 . We impose $r_s < R_{\text{vir}}$ in the fitting procedure to avoid possible divergence of γ .

3. The Einasto profile (Einasto 1965)

$$\frac{d \ln \rho}{d \ln r} = -2 \left(\frac{r}{r_{-2}} \right)^{\alpha_{\text{Einasto}}}. \quad (14)$$

This model is characterized by two parameters, r_{-2} and α_{Einasto} . To compare with the other two models,

we define

$$c_{\text{Einasto}} = \frac{R_{\text{vir}}}{r_{-2}}, \quad (15)$$

$$\gamma_{\text{Einasto}} = 2c_{\text{Einasto}}^{\alpha_{\text{Einasto}}} \text{ (slope at } R_{\text{vir}} \text{)}, \quad (16)$$

where γ_{Einasto} is the slope of the logarithmic density profile at R_{vir} and can be compared with $\gamma_{\text{NFW-like}}$.

The best fit values of these parameters are summarized in Table 2, and the comparison of the goodness-of-fit is detailed in Appendix B. For the NFW fit, our mean value agrees with Prada et al. (2011) and Bhattacharya et al. (2011). Our standard deviations are $\sigma(c)/c = 0.26$ and $\sigma(\log_{10} c) = 0.11$, which are slightly smaller than the values quoted in Bhattacharya et al. (2011) (0.33 and 0.16 based on Δ_{200c}). This difference is presumably due to the decreasing scatter in the concentration–mass relation with increasing mass; as mentioned in Bhattacharya et al. (2011), their scatter is slightly smaller for massive halos (for $M_{200} > 8 \times 10^{14} h^{-1} M_{\odot}$, the scatter is $\sigma(c)/c = 0.28$, which is very close to our value).

In the left panel of Figure 7, we add a bottom panel to compare the residual of these three models, $\langle \rho \rangle / \rho_{\text{fit}}$. Here $\rho_{\text{fit}}(r)$ is obtained by fitting the *stacked* binned density profile of all halos, and the legend shows the best-fit parameters for each model. We note that these values are slightly different from the average values of halos (shown in Table 2); i.e., the fit of the average results in slightly higher concentrations than the average of the fit to each halo. Among these three profiles, the Einasto profile fits to the stacked density profile best, deviating by up to 5%, whereas the NFW profile deviates by up to 10%. A similar trend of deviations has also been shown in the Phoenix simulations (Gao et al. 2012) and the Aquarius simulations (Navarro et al. 2010).

4.2. Density profile and formation history

We explore several aspects of the impact of the formation history on halo density profiles. In §4.2.1, we present the correlation between concentration and formation time, as well as the impact of formation time on the deviation from NFW. In §4.2.2, we show that the slope of profile also depends on formation time and that subhalos alter the slope profile of late-forming halos. We show the evolution of concentration in §4.2.3.

4.2.1. Formation time, concentration, and the deviation from NFW

Figure 4 includes c_{NFW} and the goodness-of-fit of NFW, defined as

$$\Delta_{\text{NFW}} = \max|M(< r) - M_{\text{NFW}}(< r)|/M_{\text{vir}}. \quad (17)$$

We find that both quantities are strongly correlated with $z_{1/2}$, z_{imm} , and $\gamma - \beta$, and the correlation is strongest with $z_{1/2}$. The correlation between concentration and formation time is well known (e.g., Navarro et al. 1997; Wechsler et al. 2002), and the canonical explanation is that the concentration of halos reflects the physical density of the universe at their formation epoch. The correlation between the deviation from NFW and formation time can be understood through the relaxedness of halos: late-forming halos tend to show larger deviation from NFW because of recent mergers and late-time mass accretion. Although highly concentrated clusters tend to be closer to NFW, we note that c_{NFW} and Δ_{NFW} only have a weak correlation.

To further explore the correlation between formation time and concentration, as well as the deviation from NFW, we split our halos into quartiles based on $z_{1/2}$. In the right panel of Figure 7, we present the average density profile of halos of each quartile. The upper panel shows that the formation time can lead to systematic differences in the density profile. For each average density profile, we fit the NFW profile and present the residual, $\langle \rho(r) \rangle / \rho_{\text{NFW}}$, in the bottom panel. Deviations from NFW are again systematic; around $0.1 R_{\text{vir}}$ NFW fits tend to overestimate. The latest-forming quartile tends to have the largest deviations from NFW, while the two early-forming quartiles show less deviation. We note that the deviation from NFW cannot be entirely attributed to the departure from spherical symmetry. As we will show in §6, the shape and triaxiality of halos do not strongly correlate with formation time and cannot account for the observed deviation from NFW.

4.2.2. The slope of density profile: Impact of subhalos

To further understand the impact of formation time on the deviation from NFW, we compare the logarithmic slope of the density profile in the quartiles of highest and lowest $z_{1/2}$. The left panel of Figure 8 shows the absolute value of the logarithmic slope of the density profile, $\Gamma = -d \ln \langle \rho \rangle / d \ln r$, where $\langle \rho \rangle$ is obtained by stacking halos in the highest and lowest $z_{1/2}$ quartiles. We also show the slope expected from NFW as dotted curves. The slopes deviate substantially from NFW for most radii.

The effect of formation time on the halo concentration can also be seen in the left panel of Figure 8. We mark

the location of r_s as vertical dashed lines. For early-forming halos, r_s is exactly the radius where the slope equals -2. In contrast, for late-forming halos, r_s is smaller than the radius where the slope equals -2. This indicates that the NFW model does not provide an adequate fit to their profiles, leading to the correlation between $z_{1/2}$ and Δ_{NFW} seen in Figure 4. In addition, we note that a lower Γ around $0.2 R_{\text{vir}}$ corresponds to a larger r_s , and thus a smaller NFW concentration.

In the notation of the Einasto profile,

$$\Gamma = 2 \left(\frac{r}{r-2} \right)^{\alpha_{\text{Einasto}}}, \quad (18)$$

$$\frac{d \ln \Gamma}{d \ln r} = \alpha_{\text{Einasto}}. \quad (19)$$

For early-forming halos, Γ is close to a power law; therefore, the Einasto profile provides a fit better than NFW.⁹ However, for late-forming halos, neither model provides a good fit, and the logarithmic slope of Γ has a sudden increase around $0.3 R_{\text{vir}}$. This “kink” in Γ can be explained by the presence of subhalos. In the right panel of Figure 8, we present the slope with the massive subhalos ($v_{\text{max}} > 200$ km/s) removed. After removing these subhalos, the kink in the red curve disappears, and the difference between the blue and red curves is significantly reduced.¹⁰ We also note that in the presence of a massive subhalo, the slope can be shallower near the locus of the subhalo and steeper at larger radii. Therefore, the presence of subhalos can explain the kink in the slope in Figure 8.

4.2.3. Evolution of concentration

Figure 9 shows the mean concentration evolution of our main halos. The red/blue curve corresponds to the low/high $z_{1/2}$ quartile. To emphasize the late-time phenomenon, we plot logarithmic scale factor as the x -axis. For $a < 0.6$, the averages of both populations remain relatively constant and have similar values, reflecting the split in $z_{1/2}$. For $a > 0.6$, the concentration of early-forming halos increases steadily with time and the scatter decreases; this steady increase in concentration is presumably related to the lack of significant mass growth and the resulting higher degree of relaxedness. On the other hand, the mean concentration of late-forming halos does not increase much and still shows large scatter.

The right panel of Figure 9 shows the evolution of r_s in physical h^{-1} Mpc. When the mean concentration of early-forming halos increases, the mean r_s value remains nearly constant, suggesting that the increase in concentration could be mainly driven by the pseudo-evolution of R_{vir} related to the time dependence of $\Delta_{\text{vir}} \rho_{\text{crit}}$. To confirm this, we add an inset showing the mean mass evolution

⁹ We calculate the residual for Figure 8: $\Delta_{\text{model}}^{\Gamma} = \sum_{i=1}^N |\Gamma_{\text{true}}(r_i) - \Gamma_{\text{model}}(r_i)| / \langle \Gamma_{\text{true}} \rangle$. For early-forming halos, $\Delta_{\text{NFW}}^{\Gamma} = 1.2$ and $\Delta_{\text{Einasto}}^{\Gamma} = 0.65$. For late-forming halos, $\Delta_{\text{NFW}}^{\Gamma} = 3.0$ and $\Delta_{\text{Einasto}}^{\Gamma} = 2.9$. For all halos, $\Delta_{\text{NFW}}^{\Gamma} = 1.59$ and $\Delta_{\text{Einasto}}^{\Gamma} = 1.02$.

¹⁰ Our subhalo removal procedure is based on the subhalo-particle assignment based on ROCKSTAR; different halo finders tend to have different subhalo-particle assignment criteria (e.g., see Onions et al. 2012). Since our purpose is to understand the trend with and without the presence of the subhalos, we do not expect that detailed particle assignment will impact the trend discussed here.

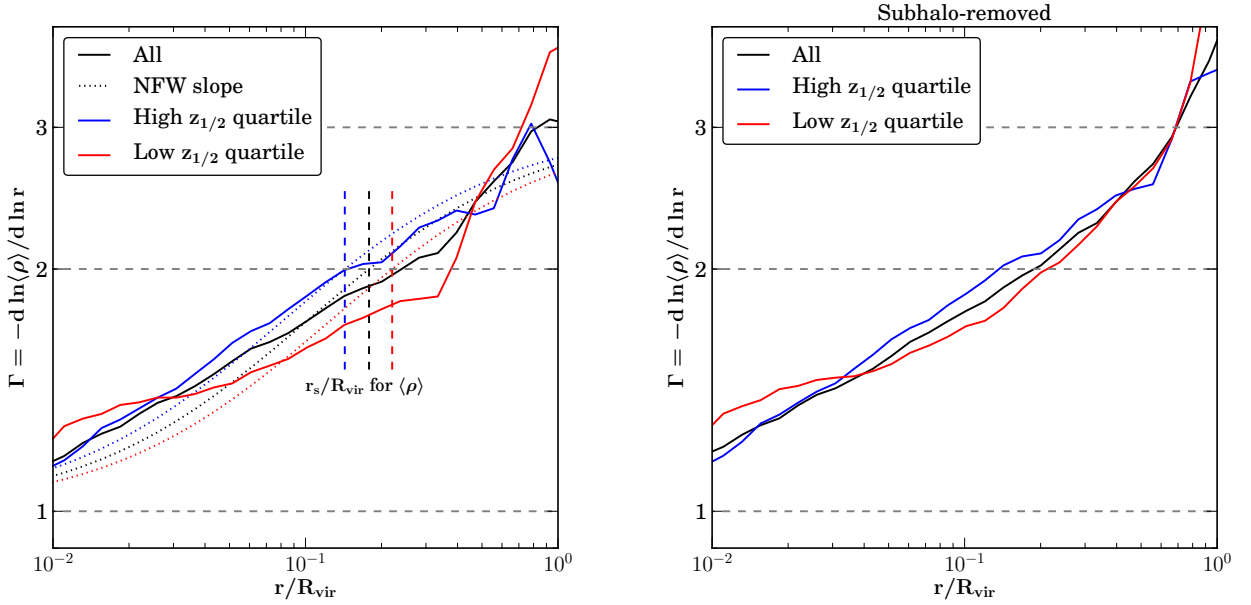


Figure 8. *Left:* The absolute value of the logarithmic slope of the density profile, Γ . The red/blue curve corresponds to the mean value of the low/high $z_{1/2}$ quartile. We also mark the r_s and slope expected from NFW. Except for the early-forming halos at around r_s , Γ deviates substantially from NFW. For late-forming halos, $\Gamma < 2$ at r_s (shallower than NFW expectation). For early-forming halos, Γ approximately follows a power law and can be well described by an Einasto profile. For late-forming halos, Γ appears to be a broken power law and suddenly increases around $0.3 R_{\text{vir}}$. *Right:* Halos with their massive subhalos ($v_{\text{max}} > 200$ km/s) removed. For late-forming halos, the kink around $0.3 R_{\text{vir}}$ disappears with the removal of subhalos, and their differences from the early-forming halos are reduced. This result indicates that the differences in Γ in the left panel are largely driven by massive subhalos.

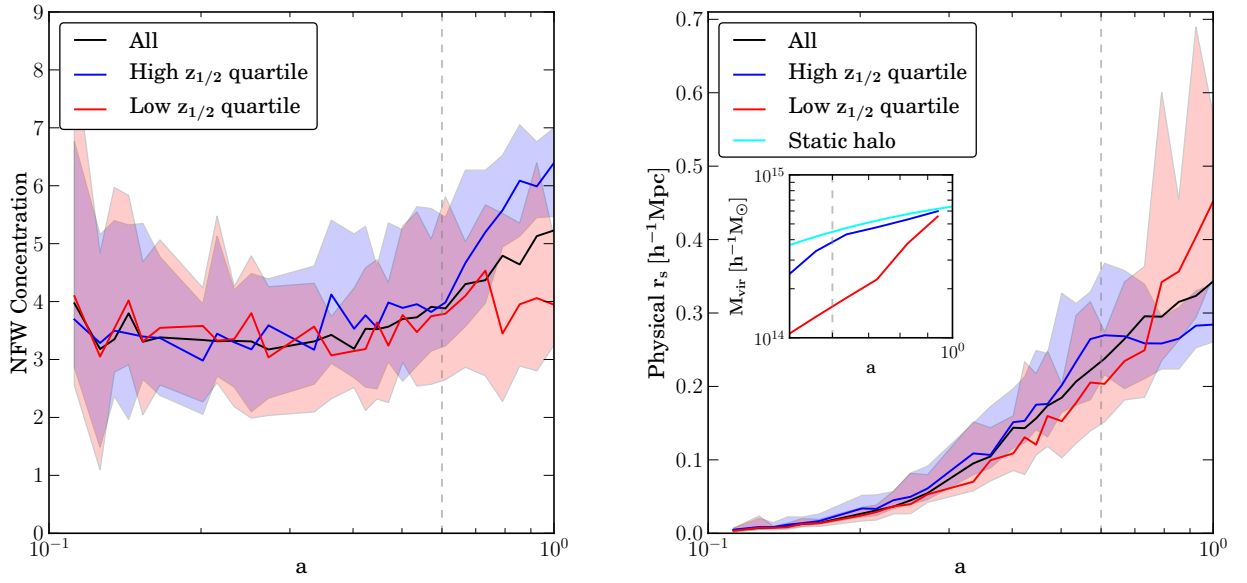


Figure 9. Evolution of NFW concentration (*left*) and scale radius (*right*). The red/blue curve corresponds to the mean of the halos in low/high $z_{1/2}$ quartile. For late-forming halos, the mean concentration remains relatively constant for all redshifts. For early-forming halos, the mean concentration remains constant at high redshift; however, for $a > 0.6$, the concentration steadily increases, while r_s remains nearly constant. In the inset, we compare their late-time mass accretion with the pseudo-evolution of a static halo, indicating that the increase in concentration of early-forming halos is largely driven by pseudo-evolution.

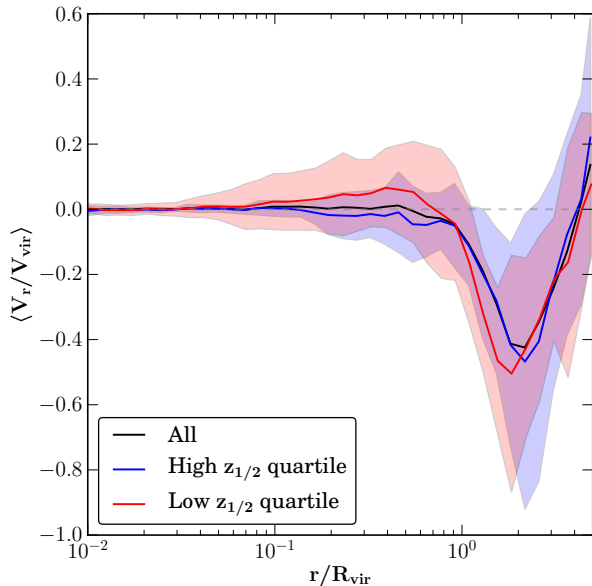


Figure 10. The mean radial velocity profiles of RHAPSODY halos. The red/blue curve corresponds to halos in the low/high $z_{1/2}$ quartile, and the band corresponds to the standard deviation of the sample. Late-forming halos show a significant outflow between 0.3 and 1 R_{vir} on average and have larger scatter. In addition, late-forming halos tend to have stronger infall than early-forming halos beyond R_{vir} . We will demonstrate that the outflow of the late-forming halos is related to the coherent motions of dark matter particles associated with subhalos.

of both populations as well as the pseudo-evolution of a static halo. As can be seen, for early-forming halos, the mass evolution for $a > 0.6$ is close to the pseudo-evolution, indicating that these halos are on average close to static and their increase in concentration is indeed driven by the pseudo-evolution. We note that the constant r_s has been shown in lower mass systems (e.g., Bullock et al. 2001; Wechsler et al. 2002), here we show that it also happens in relaxed massive halos.

5. THE IMPACT OF FORMATION TIME ON THE PHASE-SPACE STRUCTURE

In this section, we present the impact of formation time on the phase-space structure of halos. The phase-space structure has been explored for the purpose of seeking alternative definitions of halo boundary and mass (e.g., Busha et al. 2005; Cuesta et al. 2008); understanding the connection between density and velocity distribution (e.g., Hansen & Moore 2006; Navarro et al. 2010); calculating possible caustics to aid the search for lensing or dark matter annihilation signal (e.g., Diemand & Kuhlen 2008). In this work, we focus on the radial velocity profile because the infall and outflow patterns carry the information of formation and merger history and can help us understand the build-up of the density profile as well as the state of equilibrium.

Figure 10 presents the differential radial velocity profile

$$\left\langle \frac{V_r}{V_{\text{vir}}} \left(\frac{r}{R_{\text{vir}}} \right) \right\rangle \quad (20)$$

of the dark matter particles that are bound to the main halos. We again split halos by their $z_{1/2}$ and present

the halos in the highest and lowest quartiles.¹¹ The late-forming halos (red curve) show an average outflow within R_{vir} . As will be discussed in the following paragraph, these outflows are related to the coherent motions of the particles associated with recently merged subhalos. When these subhalos pass through the main halo, their particles tend to have high outflowing velocities. On the other hand, early-forming halos tend to show more regular infall patterns.

The presence of a significant fraction of particles exceeding the virial velocity of the main halo is consistent with the detection of the so-called “back-splash” population of halos (e.g., Gill et al. 2005; Ludlow et al. 2009) in the outskirts of massive halos. These halos have left the virial radius after their initial accretion onto the halo and have experienced tidal stripping much like their siblings remained inside the virial radius.

Figure 11 compares the phase-space structures for early-forming and late-forming halos. We stack the halos in the high (left panel) and low (right panel) $z_{1/2}$ quartiles and present V_r vs. r (both normalized using the virial units). These two populations show different features in the phase-space diagram. The late-forming halos again show an average outflow between 0.3 and 1 R_{vir} . In addition, in this radial range, the shapes of the contours are different. For early-forming halos, the contours are close to parallel to the x -axis; for late-forming halos, the contours are curved upward.

We find that the outflow in late-forming halos, like the kink in Γ , is related to the presence of massive subhalos. In the bottom panels of Figure 11, we remove subhalos with $v_{\text{max}} > 200$ km/s, and the outflow is reduced.

Although formation history does not strongly impact the velocity ellipsoid (as will be shown in §6.2), it clearly impacts the radial velocity profile. We also note that the outflows shown here are more likely to be found in dynamically young systems, including cluster-size systems with late formation time (like our sample) or galactic systems at high redshift.

6. SHAPES AND ALIGNMENTS

In this section, we present the shapes for the spatial distributions and velocities of dark matter particles of the main halos in RHAPSODY, as well as the alignments of their orientations. Our motivation is again related to the formation history: The accretion of matter onto massive halos is presumably correlated with the surrounding large-scale structure, and anisotropic accretion onto the halo can leave an imprint in both the shape of the halo and the motion of matter in its interior.

6.1. Halo shapes

N-body simulations have shown that dark matter halos are generally not spherical objects but have significant ellipticity and triaxiality (e.g., Jing & Suto 2002; Kasun & Evrard 2005; Allgood et al. 2006; Bett et al. 2007; Hayashi et al. 2007). Calibrations of halo shapes from simulations directly impact the accuracy of weak lensing mass calibration (e.g., Corless & King 2007; Bett 2012; Schneider et al. 2012) and can be used to constrain the

¹¹ We note that for each halo, $\langle V_r \rangle$ is itself the mean of the particles in a radial bin, and the stacking process is the average over the $\langle V_r \rangle$ of individual halos.

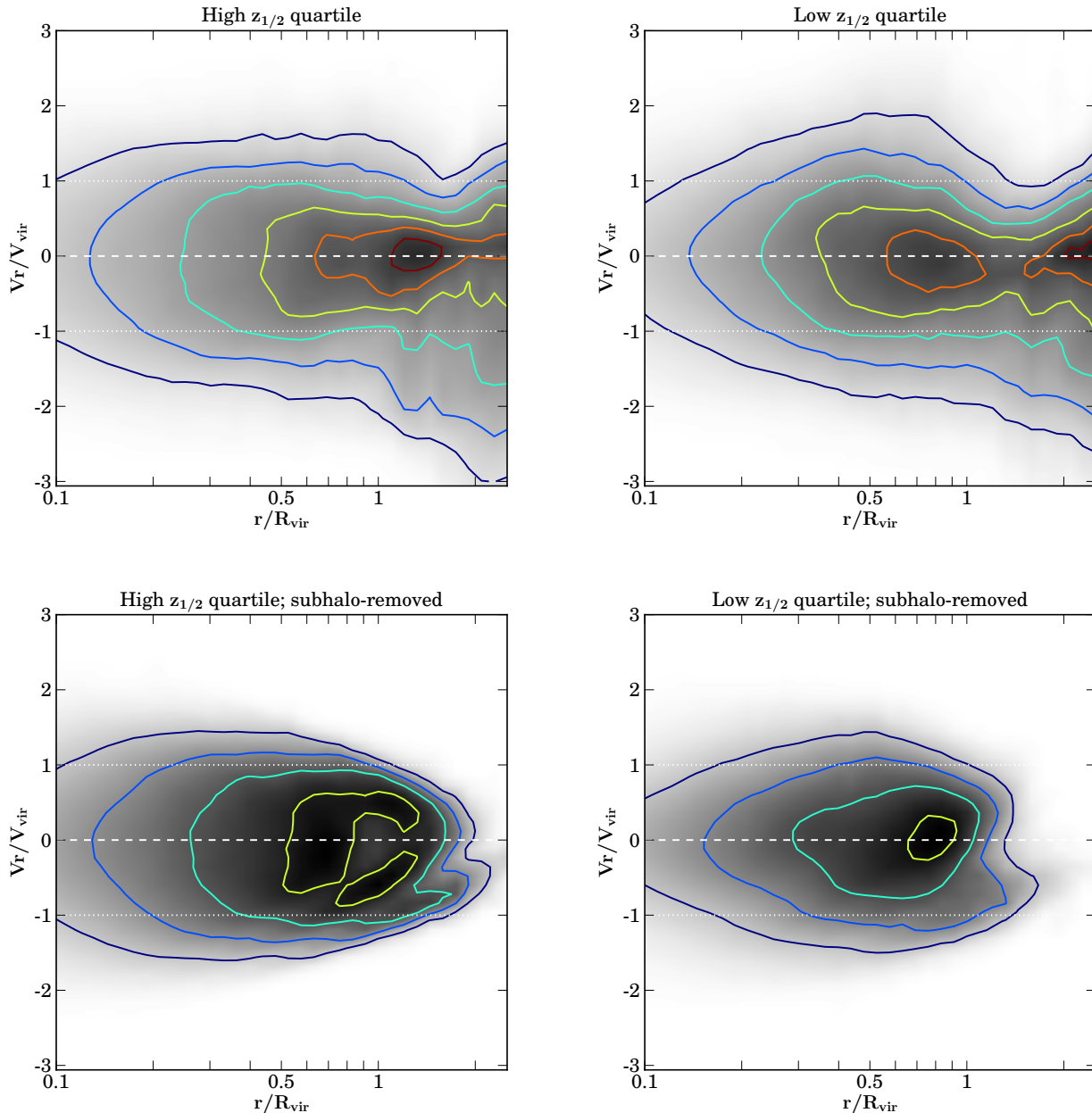


Figure 11. The impact of formation time on the phase-space structure of halos. Upper/Lower: Including/excluding subhalos. Left/Right: The high/low $z_{1/2}$ quartile. Comparing the two upper panels, we can see that the late-forming halos show stronger outflow between 0.3 and 1 R_{vir} , and the curvy shapes of the contours in this region correspond to the kink in the slope of density profile at the same scale shown in Figure 8. Comparing the two right panels, we can see that the outflow in the subhalo-removed systems is reduced.

self-interaction cross-section of dark matter particles (e.g., Miralda-Escudé 2002).

The shape parameters are typically defined through the mass distribution tensor with respect to the halo center

$$I_{ij} = \langle r_i r_j \rangle, \quad (21)$$

where r_i is the i^{th} component of the position vector \mathbf{r} of a dark matter particle with respect to the halo center, and the average $\langle \cdot \rangle$ is over all dark matter particles within R_{vir} . Since all particles within R_{vir} are of the same mass, no weighting by mass is needed. The eigenvalues of I_{ij} are sorted as $\lambda_1 > \lambda_2 > \lambda_3$, and the shape parameters are defined as $a = \sqrt{\lambda_1}$, $b = \sqrt{\lambda_2}$, $c = \sqrt{\lambda_3}$. We present

the dimensionless ratios b/a and c/a . In addition, the triaxiality parameter is defined as

$$T = \frac{a^2 - b^2}{a^2 - c^2}. \quad (22)$$

We list these halo shape properties in Table 2 and present the distribution of c/a in Figure 4. The shape parameter c/a is only weakly correlated with formation history. The correlation is even weaker for b/a and T .

It has been shown that the halo shape depends on the radius at which it is measured (e.g., Bailin & Steinmetz 2005). We also measure the halo shape at R_{500c} and find that b/a , c/a , and T measured at R_{500c} are correlated

with those measured at R_{vir} , with correlation coefficients 0.61, 0.63, and 0.60, respectively. The major axes measured with R_{500c} and R_{vir} have a median angle of 21° , which agrees with the value ($\sim 20^\circ$) reported by Schneider et al. (2012) for the Millennium Simulations.

Allgood et al. (2006) used a smaller radius $0.3R_{\text{vir}}$ and an iterative method to calculate the reduced inertia tensor (weighted by r^{-2} to suppress the influence of the larger radii). They found that c/a is correlated with formation time, and the correlation is weaker for higher mass. In our measurement with unreduced inertia tensor at R_{vir} and R_{500c} , the correlation between c/a and $z_{1/2}$ is not strong (0.27 and 0.29 respectively). Since Allgood et al. (2006) did not state the correlation coefficient and did not have statistics in our mass regime, we cannot make a direct comparison but note that the different mass regime and measurement methods could impact these correlations. Bett (2012) recently showed that the shape measured from the iterative reduced tensor is similar to and only slightly more spherical than those obtained with the simple method applied here.

Shaw et al. (2006) showed that the measured shapes depend somewhat on the state of relaxedness. For our sample of halos, we also find a weak correlation between c/a and the goodness-of-fit proxy Δ_{NFW} . While the correlation is weak, it is however interesting to note that none of our halos is close to spherical (high c/a) and has a high Δ_{NFW} at the same time. Given such a correlation, one might thus wonder whether the deviations from the NFW profile—with a strong dependence on the formation time $z_{1/2}$, as discussed in Section 4.2.3—are driven by systematic deviations from sphericity of the entire virialized halo, or by the anisotropic distribution of the most massive subhalos. To decide this, we repeat the measurements of the shape parameters after removing all subhalos with $v_{\text{max}} > 200$ km/s. We find that the correlation coefficient between Δ_{NFW} and c/a at R_{vir} drops from -0.20 to a mere 0.01 when subhalos are removed. Similarly, at R_{500c} , we observe a drop of the correlation coefficient from -0.29 to 0.05. This is strong evidence that the deviations from NFW at variance with formation time are predominantly driven by recently accreted subhalos. The correlation between shape and formation time then is a simple consequence of the anisotropic distribution of these subhalos.

6.2. Velocity ellipsoid

White et al. (2010) have demonstrated that the anisotropic motion of subhalos in clusters introduces significant scatter in the velocity dispersions measured along different lines of sight. Here we follow the same procedure to measure the properties of the velocity ellipsoid of the dark matter particles in the RHAPSODY sample.

Analogous to the mass distribution tensor, the velocity ellipsoid is defined as

$$\sigma_{ij}^2 = \langle v_i v_j \rangle. \quad (23)$$

Sorting the eigenvalues of the velocity ellipsoid as $\lambda_1 > \lambda_2 > \lambda_3$, one can again define shape parameters $a^{(v)} = \sqrt{\lambda_1}$, $b^{(v)} = \sqrt{\lambda_2}$, $c^{(v)} = \sqrt{\lambda_3}$, and dimensionless ratios $b^{(v)}/a^{(v)}$ and $c^{(v)}/a^{(v)}$ to describe the velocity ellipsoid.

The mean and scatter of the velocity dispersions mea-

sured along different lines of sight can be calculated as

$$\langle \sigma_{\text{los}}^2 \rangle = \frac{1}{3}(\lambda_1 + \lambda_2 + \lambda_3), \quad (24)$$

$$(\delta\sigma_{\text{los}}^2)^2 = \frac{4}{45}(\lambda_1^2 + \lambda_2^2 + \lambda_3^2 - \lambda_1\lambda_2 - \lambda_2\lambda_3 - \lambda_3\lambda_1). \quad (25)$$

We list these parameters in Table 2. In Figure 4, we show the distribution of $c^{(v)}/a^{(v)}$, which, like c/a , is only weakly correlated with formation time. The correlation is similar for $b^{(v)}/a^{(v)}$ and $\delta\sigma_{\text{los}}^2$.

We also measure the velocity ellipsoid based on R_{500c} . In this case, the correlation is stronger than halo shape: $b^{(v)}/a^{(v)}$, $c^{(v)}/a^{(v)}$, and $\delta\sigma_{\text{los}}^2$ measured at R_{500c} are correlated with those values measured at R_{vir} with correlation coefficients 0.80, 0.86, and 0.86, respectively. The major axes of the velocity ellipsoid measured with R_{vir} and R_{500c} have a median angle of 14° .

As expected, the ellipsoid of dark matter distribution and velocity ellipsoid are correlated. While b/a and $b^{(v)}/a^{(v)}$ have a correlation of 0.35, we find a stronger correlation between c/a and $c^{(v)}/a^{(v)}$ of magnitude 0.53. We note that the velocity ellipsoid is in general more spherical than velocity ellipsoid, this difference is related to the fact that the shape of the gravitational potential is in general more spherical than density distribution. This trend was discussed in Kasun & Evrard (2005), who used the Hubble volume simulation and defined halos based on Δ_{200c} . Although our simulation uses a different mass definition and is in a different mass regime from theirs, our axis ratios for spatial distribution and velocity are in agreement within 0.01 with theirs. In addition, the major axes of the spatial distribution and velocity ellipsoids have a median angle of 27° , which is slightly larger than the value 22° in Kasun & Evrard (2005).

We do not find significant correlation between any of these shape parameters with the environmental parameters we measured (including several halo number overdensity and nearest neighbors for several mass thresholds). In Paper II, we will repeat these measurements for the spatial distributions and velocities of subhalos and compare them with the results measured from all dark matter particles shown here.

7. SUMMARY AND DISCUSSION

We have presented the first results of the RHAPSODY project, which includes 96 cluster-size halos with mass $M_{\text{vir}} = 10^{14.8 \pm 0.05} h^{-1} M_\odot$, re-simulated from $1 h^{-3} \text{Gpc}^3$ with a resolution equivalent to 8192^3 particles in this volume. In addition to achieving high resolution and large statistics simultaneously, RHAPSODY is unique in its well-resolved subhalos and wide span of evolution history. RHAPSODY also implemented the state-of-the-art algorithms for initial conditions (MUSIC), halo finding (ROCKSTAR), and merger trees.

Our findings are summarized as follows:

- 1. Properties of the cluster halos:** We have summarized the key properties (including various mass definitions, formation history proxies, halo concentration, and shape parameters) of the 96 main halos of the RHAPSODY sample in Table 2 and shown the distributions and mutual covariance of a subset of these properties in Figure 4.

2. **Mass accretion history and merger rate:** We have investigated the mass accretion history of the main halos in §3.1, tracking the most massive progenitors over 5 decades of mass growth. We have shown that an exponential form does not provide an adequate fit to such a wide span of time, and an extra power law is needed. In §3.2, we have shown that the differential merger rate follows a power law scaling with the merger mass ratio and is independent of redshift, in agreement with earlier work based on less massive halos or smaller samples.
3. **Density profile:** In §4, we have quantified in detail how formation time impacts the halo density profile. We have shown that the deviations from the NFW model systematically depend on the formation history of the halo. Specifically, late-forming halos tend to show larger deviations from NFW. In §4.2.2, we investigate the slope of the density profile. Early-forming halos can be well described by the Einasto model. For late-forming halos, the slope appears to be a broken power law with a sudden transition around $0.3 R_{\text{vir}}$. This kink in the slope profile is related to the abundant massive subhalos in these late-forming halos. We have also shown in §4.2.3 that, for early-forming halos, the evolution of concentration between $z \sim 1$ and 0 is consistent with pseudo-evolution.
4. **Halo shape and alignment:** As discussed in §6, the shape and velocity ellipsoid of our sample is only moderately correlated with the formation history. We present the correlation and alignment of shapes and velocity ellipsoids measured at R_{vir} and R_{500c} . Our results indicate that anisotropy of the entire virialized halo alone cannot explain the deviations of the density profiles from the NFW model and its dependence on formation time.
5. **Phase-space structure and formation time:** We have provided evidence in §5 for a connection between the density profile, massive subhalos, and the formation history of the halos. When investigating the r - V_r phase space, we find that late-forming halos show evidence for large fluctuations in the radial velocities of their dark matter particles, with a considerable fraction in excess of the virial velocities, leading to an outflow of mass from these cluster halos. We associate fluctuations in the radial velocities, outflows, as well as the kink in the density profile slope with recently accreted subhalos. On the contrary, early-forming halos show a substantially more regular motion of dark matter, as expected if they are dynamically more relaxed. Our results thus indicate that the recently accreted subhalos drive the observed deviation from the NFW profile. Due to their anisotropic distributions, these subhalos also lead to a correlation between formation time and halo shape.

In Paper II, we analyze in detail the properties of the subhalo population of the cluster halos. In addition to the impact of formation time on subhalo properties, we investigate the intertwining effects from subhalo selection, stripping, and resolution of simulations.

The RHAPSODY simulation suite provides valuable information for other aspects of cluster cosmology. For example, the cluster-size halos in RHAPSODY can be further used to study the covariances between mass tracers, for example, galaxy content, dynamics of galaxies, weak gravitational lensing, X-ray, and the SZ effect. The formation history and environment of clusters can potentially impact these mass proxies systematically, either by altering the intrinsic properties of clusters or by affecting the observed properties through the line-of-sight projection. As current multi-wavelength surveys combine these different observables for cluster mass calibration, it is imperative to understand the covariances between these observables.

Our re-simulation technique can also be applied to study the “pink elephant” clusters, which refer to a handful of massive clusters recently discovered at high redshift (e.g., Jee et al. 2009; Foley et al. 2011). These clusters have stimulated a great amount of discussion about whether they pose a challenge to the current Λ CDM paradigm of cosmology (Mortonson et al. 2011; Hoyle et al. 2011). To interpret the cosmological implications of these clusters correctly, it is important to understand their mass calibration. An extension of the current RHAPSODY sample that includes a statistical sample for these massive clusters at high redshift will improve our understanding of these massive clusters. Understanding the covariances between different observable quantities and the potential biases in the mass measurements of these clusters can help us disentangle the astrophysical and cosmological implications of these clusters.

This work was supported by the U.S. Department of Energy under contract numbers DE-AC02-76SF00515 and DE-FG02-95ER40899, and by Stanford University through a Gabilan Stanford Graduate Fellowship to HW and a Terman Fellowship to RHW. Additional support was provided by SLAC-LDRD-0030-12. This work uses data from one of the LASDAMAS simulations; mock galaxy catalogs from these simulations are available at <http://lss.phy.vanderbilt.edu/lasdamas/>. We are grateful to our LASDAMAS collaborators, and especially Michael Busha, who ran the CARMEN box that was used for re-simulation; we also thank Michael for extensive helpful discussions. We thank Ralf Kaehler for assistance with visualizations of the simulations. We gratefully acknowledge the support of Stuart Marshall, Amedeo Perazzo, and the SLAC computational team, as well as the computational resources at SLAC. We also thank Gus Evrard, Eduardo Rozo, Matt Becker, Andrey Kravtsov, Sarah Hansen, Anja von der Linden, Douglas Applegate, and Will Dawson for helpful discussions and comments.

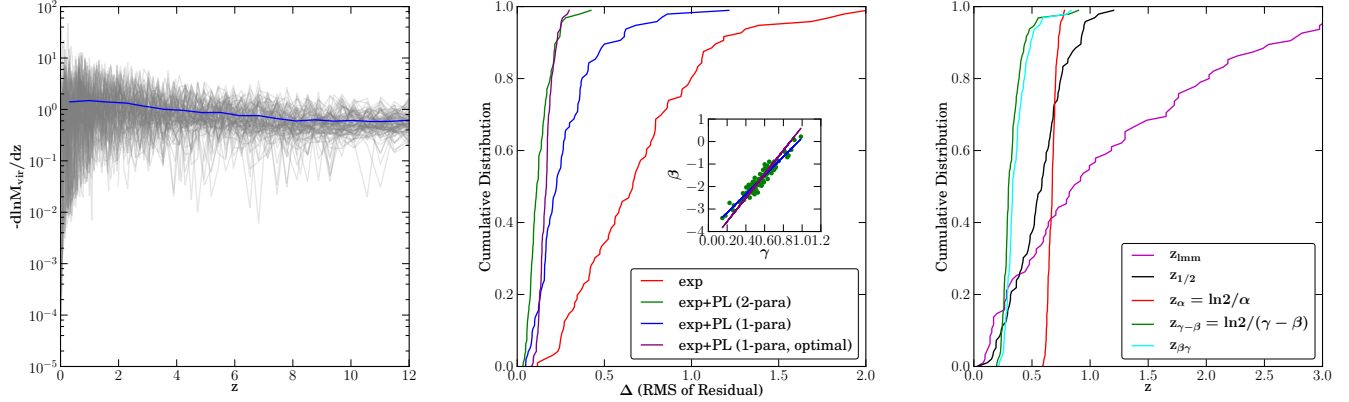


Figure 12. *Left:* The mass accretion rate of the RHAPSODY halos, $-d \ln M_{\text{vir}} / dz$, as a function of z , averaged over every 3 output redshifts to reduce the noise. *Middle:* Comparison of different fitting forms of mass accretion history: exponential model (Eq. 3) with one free parameter α ; the exponential-plus-power law model with two free parameters β and γ (Eq. 6) or one free parameter (Eq. 9). The one-parameter model using an optimal relation between β and γ (the purple curve; also see the inset) provides a compelling description of the mass accretion history. *Right:* The cumulative distribution of several proxies for formation time: $z_{1/2}$ (the exact half-mass redshift); $z_{\alpha} = \ln 2 / \alpha$; $z_{\gamma-\beta} = \ln 2 / (\gamma - \beta)$; $z_{\beta\gamma}$ (half-mass redshift obtained by solving Eq. 6). These different formation time proxies probe somewhat different epochs in a halo’s history.

APPENDIX

FITTING THE FORMATION HISTORY

For each mass accretion history model described in §3.1, we minimize the target function

$$\Delta_{\text{model}}^2 = \frac{1}{N} \sum_{i=1}^N [\log_{10} M(z_i) - \log_{10} M_{\text{model}}(z_i)]^2. \quad (\text{A1})$$

We note that this function differs from what was used in McBride et al. (2009)

$$\Delta_{\text{model}}^2 = \frac{1}{N} \sum_{i=1}^N \frac{[M(z_i)/M_0 - M_{\text{model}}(z_i)/M_0]^2}{M(z_i)/M_0}. \quad (\text{A2})$$

Because our mass accretion history spans approximately 5 orders of magnitude in mass and starts from redshift 12, weighting by $M(z_i)/M_0$ significantly underweights high redshift outputs.

The left panel of Figure 12 shows the mass growth rate defined as

$$-\frac{d \ln M_{\text{vir}}}{dz} \quad (\text{A3})$$

as a function of z . In §3.1 we have discussed the deviation of mass accretion history from a power law, and this figure clearly shows that the mass accretion rate is not constant and presents a large amount of scatter.

The middle panel presents the cumulative distribution of RMS residuals, Δ_{model} (Eq. A1), for the fits to various models of accretion history. The red curve corresponds to the exponential model, which has the largest residuals; the green curve corresponds to the exponential-plus-power law model with two free parameters (β , γ), which has the smallest residuals. In between these two models, we compare two 1-parameter models: the blue curve corresponds to the model that uses the linear fit between β and γ ($\beta = 4.16\gamma - 4.00$) to eliminate one parameter; the purple curve corresponds to an optimization of the relation between β and γ to minimize the overall residuals, obtained with several iterations. The optimal relation is given by

$$\beta = 5.27\gamma - 4.61 \quad (\text{A4})$$

This 1-parameter model performs almost equally well as the 2-parameter model does.

The right panel of Figure 12 shows the cumulative distribution functions for several halo formation time proxies:

- $z_{1/2}$, the redshift when the halo first reaches half of its final mass.
- $z_{\alpha} = \ln 2 / \alpha$, the redshift at which $M(z_{\alpha}) = M_0 / 2$ for the exponential fit.
- $z_{\gamma-\beta} = \ln 2 / (\gamma - \beta)$, analogous to z_{α} , where β and γ come from a fit to the exponential-plus-power law model (Eq. 6). We note that $z_{\gamma-\beta}$ is equivalent to the value of z_{α} measured with only the low redshift outputs.
- $z_{\beta\gamma}$, obtained by numerically solving $M(z_{\beta\gamma}) = M_0 / 2$ using the exponential-plus-power law model (Eq. 6).

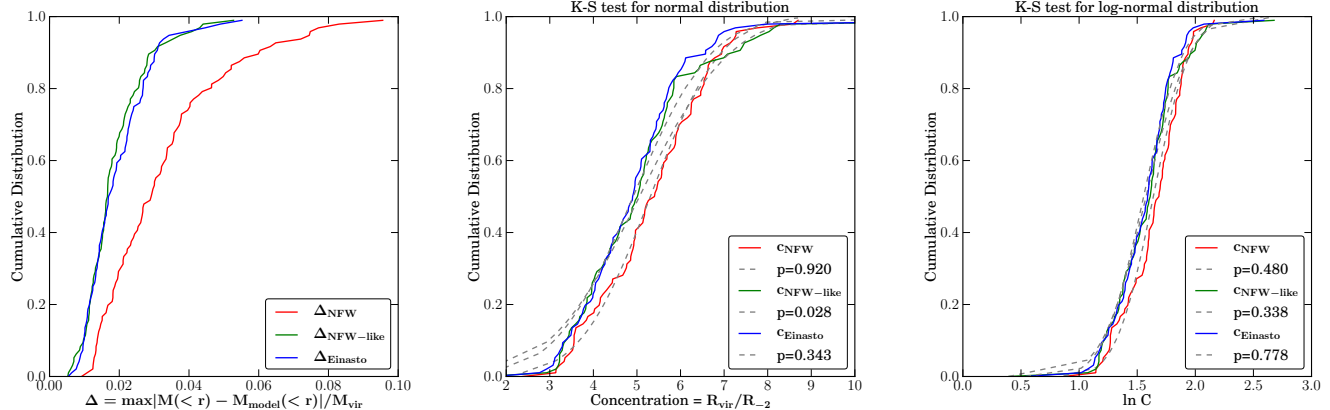


Figure 13. *Left:* The Kolmogorov–Smirnov statistics for three models for the density profile: NFW, NFW-like (with a free outer slope), and Einasto. The NFW-like and the Einasto models work equally well. *Middle and Right:* Concentration distributions based on: c_{NFW} , $c_{\text{NFW-like}}$, and $c_{\text{Einasto}} = R_{\text{vir}}/R_{-2}$. *Middle/Right* shows the cumulative distribution of $c/\ln c$ and the corresponding best-fit of normal/log-normal distribution (dashed curve). Both normal and log-normal can well describe c_{NFW} and c_{Einasto} , while $c_{\text{NFW-like}}$ prefers a log-normal distribution.

None of the formation time proxies obtained from the fitting functions captures the exact half-mass redshift. The rank correlation between z_{α} and $z_{1/2}$ is 0.55, and that between $z_{\gamma-\beta}$ and $z_{1/2}$ is 0.69. Since we fit for 5 orders of magnitude in mass growth (10^{10} to $10^{14.8} h^{-1} M_{\odot}$), these functions are not flexible enough to describe the late stage of halo evolution. Nevertheless, these different formation time definitions are still useful because they probe different epochs in a halo’s history; z_{α} tends to be a slightly earlier epoch, while $z_{\gamma-\beta}$ and $z_{\beta\gamma}$ tend to be later compared to $z_{1/2}$. Although $z_{\beta\gamma}$ is completely correlated with $z_{\gamma-\beta}$, it corresponds to a slightly earlier redshift.

FITTING THE DENSITY PROFILE: GOODNESS OF FIT

For each model described in §4, we apply the maximum-likelihood method for fitting the density profiles of individual halos. The procedure of finding the maximum-likelihood estimator is to maximize the log-likelihood function over a set of parameters, \mathbf{p} . The log-likelihood function is defined as

$$\ell(\mathbf{p}) = \frac{1}{N} \sum_i \log(\nu_{\mathbf{p}}(r_i)), \quad (\text{B1})$$

where the summation runs over all the N particles, and

$$\nu_{\mathbf{p}}(r) = \frac{1}{M} 4\pi r^2 \rho_{\mathbf{p}}(r) \quad (\text{B2})$$

so that $\int \nu_{\mathbf{p}}(r) dr = 1$. This approach is consistent with the radially-binned fitting method with a large number of particles and is more stable than using a fixed number of bins when the halo has fewer particles.

The left panel of Figure 13 presents the Kolmogorov-Smirnov statistics for these three models, where

$$\Delta_{\text{model}} = \frac{\max|M(<r) - M_{\text{model}}(<r)|}{M_{\text{vir}}} \quad (\text{B3})$$

The two-parameter models, the NFW-like and the Einasto models, work almost equally well and are significantly better than the single-parameter NFW model.

In the middle/right panel, we show the cumulative distribution for $c/\ln c$ for the three different models stated above. We also show the corresponding best fit normal/log-normal distributions and list the p-value based on a Kolmogorov-Smirnov test for goodness of fit. For the NFW and the Einasto models, both normal and log-normal distribution provide acceptable descriptions. For the NFW-like profile, a log-normal distribution provides a slightly better description.

REFERENCES

- Allen, S. W., Evrard, A. E., & Mantz, A. B. 2011, *ARA&A*, 49, 409
 Allgood, B. et al. 2006, *MNRAS*, 367, 1781
 Angulo, R. E., Springel, V., White, S. D. M., Jenkins, A., Baugh, C. M., & Frenk, C. S. 2012, arXiv:1203.3216
 Bailin, J. & Steinmetz, M. 2005, *ApJ*, 627, 647
 Behroozi, P. S., Wechsler, R. H., & Conroy, C. 2012, arXiv:1207.6105
 Behroozi, P. S., Wechsler, R. H., & Wu, H.-Y. 2011a, arXiv:1110.4372
 Behroozi, P. S., Wechsler, R. H., Wu, H.-Y., Busha, M. T., Klypin, A. A., & Primack, J. R. 2011b, arXiv:1110.4370
 Bell, E. F., Phelps, S., Somerville, R. S., Wolf, C., Borch, A., & Meisenheimer, K. 2006, *ApJ*, 652, 270
 Bett, P. 2012, *MNRAS*, 420, 3303
 Bett, P., Eke, V., Frenk, C. S., Jenkins, A., Helly, J., & Navarro, J. 2007, *MNRAS*, 376, 215
 Bhattacharya, S., Habib, S., & Heitmann, K. 2011, arXiv:1112.5479
 Böhringer, H. et al. 2004, *A&A*, 425, 367
 Boylan-Kolchin, M., Springel, V., White, S. D. M., Jenkins, A., & Lemson, G. 2009, *MNRAS*, 398, 1150
 Bryan, G. L. & Norman, M. L. 1998, *ApJ*, 495, 80

- Bullock, J. S., Kolatt, T. S., Sigad, Y., Somerville, R. S., Kravtsov, A. V., Klypin, A. A., Primack, J. R., & Dekel, A. 2001, *MNRAS*, 321, 559
- Busha, M. T., Evrard, A. E., Adams, F. C., & Wechsler, R. H. 2005, *MNRAS*, 363, L11
- Corless, V. L. & King, L. J. 2007, *MNRAS*, 380, 149
- Crocce, M., Pueblas, S., & Scoccimarro, R. 2006, *MNRAS*, 373, 369
- Cuesta, A. J., Prada, F., Klypin, A., & Moles, M. 2008, *MNRAS*, 389, 385
- De Lucia, G. & Blaizot, J. 2007, *MNRAS*, 375, 2
- Diemand, J. & Kuhlen, M. 2008, *ApJ*, 680, L25
- Diemand, J., Kuhlen, M., Madau, P., Zemp, M., Moore, B., Potter, D., & Stadel, J. 2008, *Nature*, 454, 735
- Diemer, B., More, S., & Kravtsov, A. 2012, arXiv:1207.0816
- Ebeling, H., Edge, A. C., Allen, S. W., Crawford, C. S., Fabian, A. C., & Huchra, J. P. 2000, *MNRAS*, 318, 333
- Ebeling, H., Edge, A. C., Mantz, A., Barrett, E., Henry, J. P., Ma, C. J., & van Speybroeck, L. 2010, *MNRAS*, 407, 83
- Einasto, J. 1965, *Trudy Inst. Astrofiz. Alma-Ata*, 51, 87
- Ettori, S., Gastaldello, F., Leccardi, A., Molendi, S., Rossetti, M., Buote, D., & Meneghetti, M. 2010, *A&A*, 524, A68
- Fakhouri, O. & Ma, C.-P. 2008, *MNRAS*, 386, 577
- Fakhouri, O., Ma, C.-P., & Boylan-Kolchin, M. 2010, *MNRAS*, 406, 2267
- Foley, R. J. et al. 2011, *ApJ*, 731, 86
- Gao, L., Navarro, J. F., Cole, S., Frenk, C. S., White, S. D. M., Springel, V., Jenkins, A., & Neto, A. F. 2008, *MNRAS*, 387, 536
- Gao, L., Navarro, J. F., Frenk, C. S., Jenkins, A., Springel, V., & White, S. D. M. 2012, arXiv:1201.1940
- Gao, L., White, S. D. M., Jenkins, A., Frenk, C. S., & Springel, V. 2005, *MNRAS*, 363, 379
- Genel, S., Genzel, R., Bouché, N., Naab, T., & Sternberg, A. 2009, *ApJ*, 701, 2002
- Ghigna, S., Moore, B., Governato, F., Lake, G., Quinn, T., & Stadel, J. 1998, *MNRAS*, 300, 146
- Gill, S. P. D., Knebe, A., & Gibson, B. K. 2005, *MNRAS*, 356, 1327
- Hahn, O. & Abel, T. 2011, *MNRAS*, 415, 2101
- Hahn, O., Porciani, C., Carollo, C. M., & Dekel, A. 2007, *MNRAS*, 375, 489
- Hansen, S. H. & Moore, B. 2006, *New Astronomy*, 11, 333
- Hansen, S. M., Sheldon, E. S., Wechsler, R. H., & Koester, B. P. 2009, *ApJ*, 699, 1333
- Hao, J., McKay, T. A., Koester, B. P., Rykoff, E. S., Rozo, E., Annis, J., Wechsler, R. H., Evrard, A., Siegel, S. R., Becker, M., Busha, M., Gerdes, D., Johnston, D. E., & Sheldon, E. 2010, *ApJS*, 191, 254
- Harker, G., Cole, S., Helly, J., Frenk, C., & Jenkins, A. 2006, *MNRAS*, 367, 1039
- Hayashi, E., Navarro, J. F., & Springel, V. 2007, *MNRAS*, 377, 50
- Hopkins, P. F., Hernquist, L., Cox, T. J., Di Matteo, T., Robertson, B., & Springel, V. 2006, *ApJS*, 163, 1
- Hoyle, B., Jimenez, R., & Verde, L. 2011, *Phys. Rev. D*, 83, 103502
- Jee, M. J. et al. 2009, *ApJ*, 704, 672
- Jing, Y. P. & Suto, Y. 2002, *ApJ*, 574, 538
- Kasun, S. F. & Evrard, A. E. 2005, *ApJ*, 629, 781
- Kauffmann, G. & Haehnelt, M. 2000, *MNRAS*, 311, 576
- King, L. J. & Mead, J. M. G. 2011, *MNRAS*, 416, 2539
- Klypin, A. A., Trujillo-Gomez, S., & Primack, J. 2011, *ApJ*, 740, 102
- Knebe, A. et al. 2011, *MNRAS*, 415, 2293
- Koester, B. P. et al. 2007, *ApJ*, 660, 239
- Kravtsov, A. & Borgani, S. 2012, arXiv:1205.5556
- Lacey, C. & Cole, S. 1993, *MNRAS*, 262, 627
- Li, Y., Mo, H. J., & Gao, L. 2008, *MNRAS*, 389, 1419
- Lotz, J. M. et al. 2008, *ApJ*, 672, 177
- Ludlow, A. D., Navarro, J. F., Springel, V., Jenkins, A., Frenk, C. S., & Helmi, A. 2009, *ApJ*, 692, 931
- Macciò, A. V., Dutton, A. A., & van den Bosch, F. C. 2008, *MNRAS*, 391, 1940
- Mantz, A., Allen, S. W., & Rapetti, D. 2010a, *MNRAS*, 406, 1805
- Mantz, A., Allen, S. W., Rapetti, D., & Ebeling, H. 2010b, *MNRAS*, 406, 1759
- Marriage, T. A. et al. 2011, *ApJ*, 737, 61
- Maulbetsch, C., Avila-Reese, V., Colín, P., Gottlöber, S., Khalatyan, A., & Steinmetz, M. 2007, *ApJ*, 654, 53
- McBride, J., Fakhouri, O., & Ma, C.-P. 2009, *MNRAS*, 398, 1858
- Merritt, D., Graham, A. W., Moore, B., Diemand, J., & Terzić, B. 2006, *AJ*, 132, 2685
- Miralda-Escudé, J. 2002, *ApJ*, 564, 60
- Moore, B., Ghigna, S., Governato, F., Lake, G., Quinn, T., Stadel, J., & Tozzi, P. 1999, *ApJ*, 524, L19
- Moore, B., Governato, F., Quinn, T., Stadel, J., & Lake, G. 1998, *ApJ*, 499, L5
- Mortonson, M. J., Hu, W., & Huterer, D. 2011, *Phys. Rev. D*, 83, 023015
- Navarro, J. F., Frenk, C. S., & White, S. D. M. 1997, *ApJ*, 490, 493
- Navarro, J. F. et al. 2004, *MNRAS*, 349, 1039
- . 2010, *MNRAS*, 402, 21
- Neistein, E. & Dekel, A. 2008, *MNRAS*, 383, 615
- Neto, A. F. et al. 2007, *MNRAS*, 381, 1450
- Onions, J. et al. 2012, *MNRAS*, 423, 1200
- Planck Collaboration, Ade, P. A. R., et al. 2011, *A&A*, 536, A8
- Postman, M. et al. 2011, arXiv:1106.3328
- Prada, F., Klypin, A. A., Cuesta, A. J., Betancort-Rijo, J. E., & Primack, J. 2011, arXiv:1104.5130
- Press, W. H. & Schechter, P. 1974, *ApJ*, 187, 425
- Rapetti, D., Allen, S. W., Mantz, A., & Ebeling, H. 2010, *MNRAS*, 406, 1796
- Rapetti, D., Blake, C., Allen, S. W., Mantz, A., Parkinson, D., & Beutler, F. 2012, arXiv:1205.4679
- Reed, D., Governato, F., Quinn, T., Gardner, J., Stadel, J., & Lake, G. 2005, *MNRAS*, 359, 1537
- Reed, D. S., Smith, R. E., Potter, D., Schneider, A., Stadel, J., & Moore, B. 2012, arXiv:1206.5302
- Reid, B. A., Verde, L., Jimenez, R., & Mena, O. 2010, *Journal of Cosmology and Astroparticle Physics*, 1, 3
- Roza, E., Bartlett, J. G., Evrard, A. E., & Rykoff, E. S. 2012, arXiv:1204.6305
- Roza, E. et al. 2007, astro-ph/0703571
- . 2010a, *ApJ*, 708, 645
- . 2010b, *ApJ*, 708, 645
- Rykoff, E. S. et al. 2012, *ApJ*, 746, 178
- Schneider, M. D., Frenk, C. S., & Cole, S. 2012, *J. Cosmol. Astropart. Phys.*, 5, 30
- Shaw, L. D., Weller, J., Ostriker, J. P., & Bode, P. 2006, *ApJ*, 646, 815
- Springel, V. 2005, *MNRAS*, 364, 1105
- Springel, V. et al. 2008, *MNRAS*, 391, 1685
- Stewart, K. R., Bullock, J. S., Barton, E. J., & Wechsler, R. H. 2009, *ApJ*, 702, 1005
- Tasitsiomi, A., Kravtsov, A. V., Gottlöber, S., & Klypin, A. A. 2004, *ApJ*, 607, 125
- Tinker, J. L., Kravtsov, A. V., Klypin, A., Abazajian, K., Warren, M., Yepes, G., Gottlöber, S., & Holz, D. E. 2008, *ApJ*, 688, 709
- Tormen, G., Bouchet, F. R., & White, S. D. M. 1997, *MNRAS*, 286, 865
- van den Bosch, F. C. 2002, *MNRAS*, 331, 98
- Vikhlinin, A. et al. 2009, *ApJ*, 692, 1060
- von der Linden, A. et al. 2012, arXiv:1208.0597
- Wechsler, R. H., Bullock, J. S., Primack, J. R., Kravtsov, A. V., & Dekel, A. 2002, *ApJ*, 568, 52
- Wechsler, R. H., Zentner, A. R., Bullock, J. S., Kravtsov, A. V., & Allgood, B. 2006, *ApJ*, 652, 71
- White, M., Cohn, J. D., & Smit, R. 2010, *MNRAS*, 407, 1221
- Williamson, R. et al. 2011, *ApJ*, 738, 139
- Wu, H., Hahn, O., Wechsler, R., Behroozi, P., & Mao, Y. 2012, (Paper II), to be submitted
- Xu, C. K., Zhao, Y., Scoville, N., Capak, P., Drory, N., & Gao, Y. 2012, *ApJ*, 747, 85
- Zhao, D. H., Jing, Y. P., Mo, H. J., & Börner, G. 2009, *ApJ*, 707, 354
- Zhao, D. H., Mo, H. J., Jing, Y. P., & Börner, G. 2003, *MNRAS*, 339, 12